Tribology International 226 (2027) 112518

Contents lists available at ScienceDirect

Tribology International

journal homepage: www.elsevier.com/locate/triboint

Full Length Article

How surface roughness affects rubber friction beyond the spectrum

Stefano Avolio [a], Matthias Wangenheim [b], Andrea Ronchi [c], Antonio Serra [c], Francesco Timpone [a], Andrea Genovese [a],*

[a] Department of Industrial Engineering, University of Naples Federico II, Via Claudio, 21, Naples, 80125, Italy
[b] Institute of Dynamics and Vibration Research, Leibniz Universität Hannover, An der Universität 1, Garbsen, 30823, Germany
[c] Pirelli Tyre S.P.A., Viale Piero e Alberto Pirelli, 25, Milano, 20126, Italy

ARTICLE INFO

Keywords:
Rubber friction
Surface roughness
Tyre–road interaction
Power spectral density (PSD)
Probability density function (PDF)
3D-printed test surfaces

ABSTRACT

Friction between rubber and rough surfaces is a critical topic for vehicle safety, yet it remains unclear which roughness parameters govern it. While the power spectral density (PSD) describes the wavelength content of surface asperities, it is not known whether PSD alone predicts friction or if the height distribution (PDF) also plays a significant role. To address this, we performed dry-contact and boundary-lubricated friction tests on 3D-printed surfaces designed to share identical PSDs but different PDFs. This approach allowed us to isolate the effect of height distribution while keeping the spectral content constant. The tests revealed substantial differences in total friction despite identical PSDs, demonstrating that the PDF and related roughness parameters significantly influence rubber–road interaction. To support the interpretation of the experimental findings, the results were further compared with spectrum-based friction theories and qualitative Boundary Element Method (BEM) contact simulations. While PSD-based approaches correctly reproduced the hysteretic trends, the BEM analysis revealed systematic differences in contact-area evolution among surfaces sharing identical PSDs but different PDFs, showing qualitative consistency with the experimentally observed friction ranking. Direct measurements of the contact area using pressure-sensitive films further confirmed these differences, suggesting that contact-area evolution is the main mechanism underlying the observed dry-friction variability. These findings provide new experimental evidence beyond the PSD and have implications for tyre design and predictive friction models.

1. Introduction

The study of surface topography has a dramatic impact on the tribological field. When two bodies are in contact, their shape is really significant. Surface roughness affects how the parts interact with each other, how fluids or lubricants wet the parts, how friction affects the contact and the sliding, how heat is generated, and how the parts wear out. Therefore, accurately characterising and controlling these surface features is essential, especially as contact scales down to micro-levels. In fact, over the years, it has become necessary to measure the surfaces and look at the acquired profiles to obtain information from them [1].

The situation is no different in the automotive world, especially when we talk about the tyre-road interaction. Understanding how surface roughness affects rubber-surface interaction is the challenge of several researchers both to estimate friction and wear of compounds [2–8]. Moreover when it comes to motorsport, significant aspect of the contact is how the temperature increase at the interface among the rubber and the surface and how its characteristics influence the rubber temperature, which in turn affects friction and wear of the tyre tread during their life [9–11].

These aspects turn into extremely important concepts for vehicle safety and for increasing the performance of racing cars [12–16], thus for these reasons, these fields are of particular interest to tyre and vehicle manufacturers, as estimating friction and wear before producing the final tyre could save time, money, and reduce particulate emissions [17–19]. It is well known that different contributions rule the friction coefficient between rubber and surface: Adhesive, hysteretic, fluid, and abrasive. The most relevant are the first two [4,20]. Some authors say that they are strictly connected, and they call it “Adhesive hysteresis” [21–23]. This has led to the development of different friction and wear models, based on the knowledge about the two objects in contact, the viscoelastic part, and the road part. Using these, several attempts were made to predict the friction coefficient; whether the temperature contribution was taken into account depends on the

* Corresponding author.
E-mail addresses: stefano.avolio@unina.it (S. Avolio), wangenheim@ids.uni-hannover.de (M. Wangenheim), andrea.ronchi@pirelli.com (A. Ronchi), antonio.serra@pirelli.com (A. Serra), francesco.timpone@unina.it (F. Timpone), andrea.genovese2@unina.it (A. Genovese).

https://doi.org/10.1016/j.triboint.2026.112518
Received 29 May 2026; Received in revised form 22 July 2026; Accepted 24 July 2026
Available online 29 July 2026
0301-679X/© 2026 The Authors. Published by Elsevier Ltd. This is an open access article under the CC BY-NC-ND license (http://creativecommons.org/licenses/by-nc-nd/4.0/).

complexity of the models or on the type of experimental validation that was sought [3,20,24–27].

Many friction models attribute the prediction of friction at the road spectrum, and in particular, to the Power Spectral Density (PSD). But is the PSD sufficient on its own to describe rubber friction, or can additional roughness parameters play a complementary role?

In recent years, several theoretical approaches have attempted to relate rubber friction and contact mechanics predominantly to the spectral content of surface roughness. In particular, spectrum-based formulations, such as Persson's theory and related approaches, primarily describe frictional behaviour through the surface PSD and the viscoelastic response of rubber [3,4,20]. However, the extent to which additional morphological descriptors associated with the statistical height distribution may influence friction and contact evolution remains not fully clarified.

Previous investigations, such as the work by Fortunato et al. [28], explored numerically generated rough surfaces with comparable power spectral densities but different skewness values, showing that variations in surface asymmetry can influence frictional behaviour. The present study instead advances a systematic and experimentally validated framework for analysing morphology-induced effects. Here, surfaces were not only numerically generated but also physically reproduced, verified, and tested, ensuring full repeatability and metrological reliability. This approach extends the analysis from skewness to the entire probability density function (PDF), providing a robust and traceable methodology to quantify how height distribution influences friction once the spectral content (PSD) is fixed. To the best of our knowledge, no systematic studies have been conducted on surfaces specifically designed to share the same PSD while differing in their statistical morphology. The present work addresses this gap by introducing a controlled methodology that combines numerical generation, 3D printing, and experimental validation to reliably assess how the height distribution influences rubber friction once the PSD is fixed and experimentally investigates whether the PDF of a rough surface plays a role in rubber friction.

It is common to observe how virtual modelling can recreate surfaces with different characteristics [29], and several approaches have been proposed in the literature, such as reproducing surfaces from the fast Fourier transformation or directly from the height distribution [30–32].

Building on these concepts, seven such surfaces were generated in this work, fabricated via 3D printing, and their topographies were validated. These specimens were then tested under both dry and lubricated conditions, enabling the separation of the hysteretic component of friction.

Friction measurements carried out with a linear tester revealed that, despite having the same PSD, the surfaces exhibited different coefficients of friction. This result highlights that not only the spectral content but also the morphological characteristics of the surface, as captured by the PDF and related roughness parameters, significantly influence rubber friction. In addition, the experimental campaign allowed us to evaluate how sliding velocity, lubrication state, nominal pressure, and compound formulation affect frictional behaviour. The results show that oil lubrication selectively suppresses adhesion, the variation of load influences contact saturation across surfaces, and different viscoelastic compounds respond distinctly to the same surface morphology.

To support the interpretation of the experimental observations, the results were further compared with spectrum-based friction theories and with qualitative Boundary Element Method (BEM) contact simulations. This combined experimental–numerical approach made it possible to assess whether surfaces sharing the same PSD but different PDFs could exhibit different evolutions of the real contact area and contact saturation behaviour, thereby providing a physically consistent interpretation of the experimentally observed friction variability.

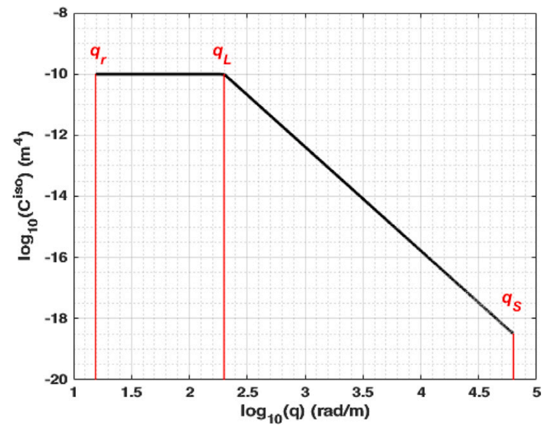

Fig. 1. Analytic PSD with lower cutoff q_r, roll-off q_L, and upper cutoff q_s.

2. Power spectral density and friction models

The PSD is defined as the Fourier transform of the autocorrelation function of the surface signal, and it has been extensively discussed in the literature [33,34]. For this reason, we do not provide a rigorous definition here. Instead, we focus on the practical approach used to compute the PSD from surface topographies and, in the specific case of this work, on the form imposed to generate synthetic surfaces.

For self-affine surfaces, the PSD follows a power-law dependence that is truncated at both low and high spatial frequencies [35,36]. The PSD $C(q)$ represents the distribution of roughness amplitude as a function of the wavevector $q = 2\pi/\lambda$, where λ is the spatial wavelength of the surface asperities: large values of λ correspond to long-wavelength features (macroscopic undulations), while small values of λ correspond to fine-scale roughness.

$$C(q) = C_0 \begin{cases} q_L^{-2-2H} = \text{const} & \text{if } q_r \le q < q_L \\ q^{-2-2H} & \text{if } q_L \le q < q_s \end{cases} \tag{1}$$

where C_0 is a normalisation constant that determines the overall amplitude of the spectrum, q_r is the lower cutoff wavevector related to the largest wavelengths of the surface, q_L is the roll-off wavevector below which the PSD becomes flat, q_s is the upper cutoff wavevector associated with the smallest roughness scales, and H is the Hurst exponent that governs the slope of the power-law regime. Larger values of H correspond to smoother surfaces at small scales.

In this way, one can construct a spectrum with both a plateau and self-affine scaling, as illustrated in Fig. 1.

The PSD of the generated surfaces was computed using a numerical algorithm for the discrete Fourier transform, which is widely adopted in the literature [35,37].

Over the past decades, several tribological models have attempted to predict rubber–road friction, with many of them converging on the role of the PSD as a fundamental descriptor of surface roughness [3,4,20,38,39]. The PSD provides the spectral distribution of the harmonic components that constitute the surface and has traditionally been regarded as the key parameter to correlate substrate morphology with the viscoelastic response of rubber within spectrum-based modelling frameworks. For this reason, its determination has become a preliminary and necessary step in friction modelling and in the analysis of tyre–road interaction when the description is limited to spectral information [33,35,40–42].

A major limitation of this approach is that the PSD, being derived from the sum of harmonic components without phase information, carries no details about the surface height distribution [35]. As a result, it does not capture whether asperities are arranged symmetrically, sharply peaked, flat or skewed, so that different surfaces may exhibit identical PSDs but still differ significantly in their morphology, with distinct values of roughness parameters such as skewness and kurtosis [43].

This limitation becomes particularly relevant when analysing rough surfaces such as road pavements, where contact occurs only on the highest asperities. To overcome this, the concept of the *Top PSD* has been introduced in the literature, i.e., the PSD calculated only from the portion of the surface above the mean plane [44]. This representation is motivated by the fact that, when rubber slides on a rough surface, it interacts mainly with the asperities protruding above the mean plane. However, the actual penetration depth of the rubber under operating conditions remains uncertain [4], making it impossible to precisely determine which portion of the surface effectively contributes to the Top PSD.

This raises a fundamental question: if the PSD captures the spectral content of roughness but ignores the statistical distribution of heights, is it sufficient to describe rubber–road friction, or should it be complemented by additional topographical descriptors? In other words, once the PSD is fixed, can the PDF of heights and related roughness parameters independently affect the frictional response?

The literature does not yet provide a conclusive answer to this question. Existing experimental validations of friction theories have typically been carried out on surfaces with different spectral contents [36,45,46], making it difficult to isolate the role of the height distribution.

In this context, it is useful to briefly analyse how current spectrum-based friction formulations interpret surfaces characterised by identical PSDs. Since the present experimental campaign was specifically designed to isolate the influence of the height distribution while preserving the spectral content, this discussion provides an important theoretical reference framework for interpreting the experimental findings.

Among the available spectrum-based approaches, Persson's theory is one of the most widely adopted formulations for describing rubber friction on rough surfaces. In the present analysis, we focus on the hysteretic contribution to friction rather than on the total friction coefficient. As discussed by Genovese et al. [47], in Persson's model, the adhesive contribution is typically determined through empirical fitting of experimental data. Consequently, its use for predictive comparisons between surfaces with different morphological features is limited.

Persson defines the ratio between the real contact area and the nominal contact area in his pioneering study [20] as:

$$\frac{A_c}{A_0} = erf\left(\frac{1}{2\sqrt{\frac{1}{8}\int_{q_0}^{q_1} q^3 C(q) \int_0^{2\pi} \left|\frac{E(q\,v\,cos\varphi)}{(1-\nu^2)\sigma_0}\right|^2 d\varphi dq}}\right) \quad (2)$$

where A_c and A_0 denote the real and nominal contact areas, respectively. From Eq. (2), it is evident that the variation of this ratio depends on the wavevector q and on the PSD $C(q)$. Since the investigated surfaces were specifically generated to exhibit overlapping PSDs, the quantities entering the formulation remain essentially identical across the different surfaces once the testing conditions and the rubber compound are fixed.

Persson further introduces a correction factor to account for the fact that rubber does not fully penetrate the surface roughness:

$$S(q) = \gamma + (1-\gamma)P^2(q) \quad (3)$$

where $\gamma = 1/2$ and $P(q) = A_c/A_0$. Since $P(q)$ remains essentially identical across the investigated surfaces, the correction factor $S(q)$ is also predicted to be nearly the same.

The hysteretic friction coefficient is then expressed as:

$$\mu_{hys} = \frac{1}{2}\int_{q_0}^{q_1} q^3 C(q)\, S(q)\, P(q) \int_0^{2\pi} cos(\varphi) Im\left(\frac{E(qvcos(\varphi))}{(1-\nu^2)\,\sigma_0}\right) d\varphi dq \quad (4)$$

This expression again depends predominantly on the PSD and on the viscoelastic response of the rubber compound. Consequently, for surfaces sharing overlapping and indistinguishable PSDs, Persson's model predicts no significant differences in the hysteretic friction contribution among the different surfaces. This outcome is fully consistent with the experimental results reported in Fig. 16, where the lubricated tests do not exhibit a clear surface-dependent ranking.

It is important to clarify that, in their current formulation, spectrum-based theories such as Persson's model do not explicitly account for the influence of the height distribution. Therefore, the absence of PDF effects in such models should not be interpreted as evidence that these effects are physically negligible, but rather as a limitation of the current theoretical framework.

It should also be noted that the present theoretical discussion inherits the simplifying assumptions of the adopted spectrum-based formulation. In particular, the viscoelastic response is evaluated without explicitly accounting for frictional heating and flash-temperature effects [10], which may become increasingly relevant as sliding velocity increases. The objective of this comparison is therefore not to provide a fully predictive description of rubber friction, but rather to assess whether the spectral content alone is sufficient to explain the experimentally observed differences between surfaces sharing the same PSD. Since flash-temperature effects are not expected to depend on the surface PDF within the adopted framework, neglecting them does not alter the main conclusion of the present comparison, namely that current spectrum-based models cannot distinguish between surfaces having identical PSDs but different height distributions.

This aspect has already been discussed in contact-mechanics literature through extensions of Greenwood–Williamson-type approaches to non-Gaussian surfaces. McCool, for instance, introduced Weibull-type height distributions and showed that surfaces sharing the same RMS roughness but differing in skewness can develop significantly different real contact areas at the same nominal load [48]. Similar conclusions were drawn in later asymmetric and non-Gaussian extensions of GW-type models [49–51], which demonstrated that skewness and kurtosis influence asperity activation, load sharing, and contact-area evolution.

Taken together, these studies suggest that surfaces with identical PSDs may still exhibit different contact mechanics behaviour due to differences in their statistical height distribution. This consideration represents the main motivation behind the experimental methodology adopted in the present work.

3. Algorithm for surface generation

The numerical generation of rough surfaces has been widely discussed in the literature [29], with several consolidated approaches. Among them, the method by Hu and Tonder is based on filtering and convolution applied to Gaussian surfaces generated via FFT [30,31]. While effective in producing non-Gaussian height distributions, this approach is relatively computationally demanding, as it requires multiple sequential steps and does not always converge efficiently towards surfaces with prescribed skewness and kurtosis values.

A more efficient alternative is the iterative scheme proposed by Almqvist [32], which progressively corrects both PSD and PDF through a ranking-order process. In this case, convergence is generally assessed by combining PSD and PDF error metrics, without the need for additional filtering operations as in Hu's method.

An interesting application of Almqvist's method was presented in [52], where the authors reconstructed virtual road surfaces directly from experimental measurements. In this case, the measured PSD and the height distribution (PDF) were used as inputs to the algorithm, with an additional slope-correction step introduced to better reproduce the localised microscale roughness. This highlights how the iterative approach can be applied not only to artificial surface generation but also to the faithful reproduction of real road textures.

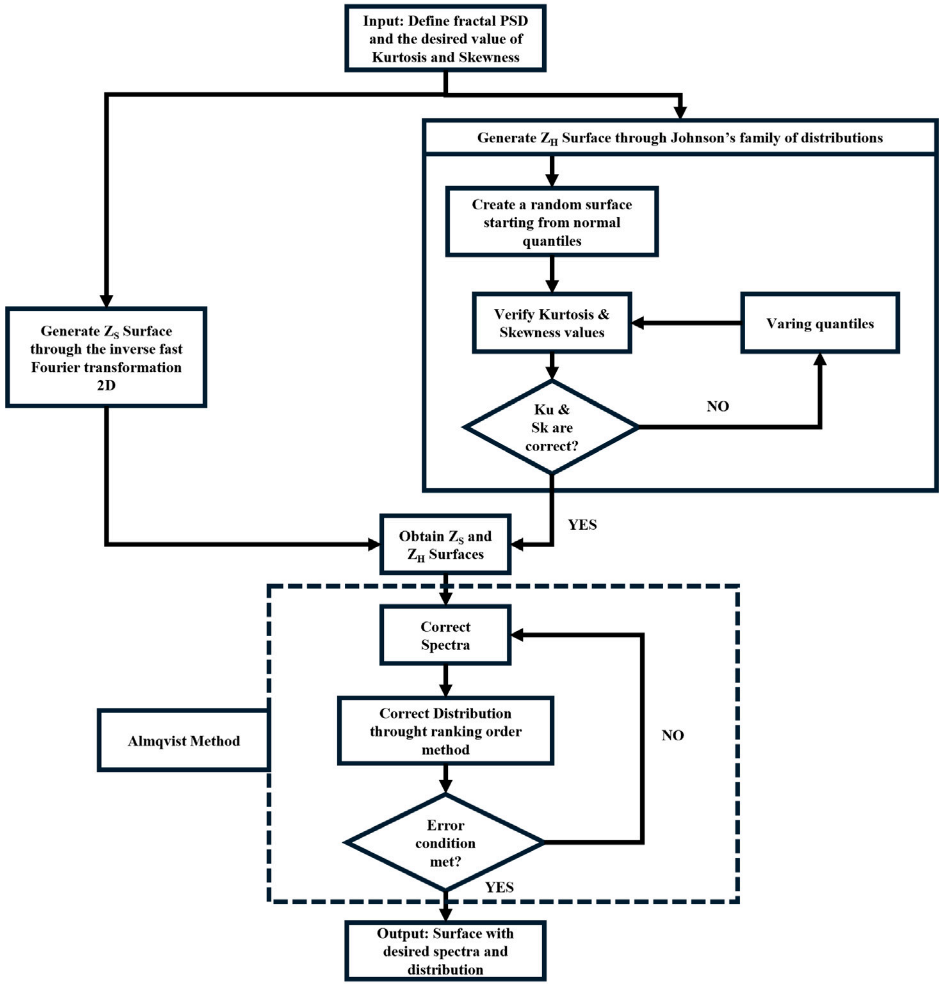

Fig. 2. Flowchart of the hybrid surface-generation algorithm combining Almqvist's iterative PSD–PDF matching procedure with Johnson's statistical transformation. The process iteratively corrects both the spectral and statistical properties of the surface until the desired PSD and PDF are simultaneously achieved.

In this work, a hybrid strategy was adopted, combining the efficiency of Almqvist's iterative procedure with the flexibility of Johnson's family of distributions to impose specific skewness and kurtosis values, whose classification and selection were formalised by Slifker and Shapiro [53].

This approach enables the controlled generation of bell-shaped height distributions—particularly representative of real road surfaces—while preserving the imposed spectral characteristics.

The workflow of the hybrid algorithm implemented in this study is illustrated in Fig. 2.

The practical innovation of this method lies in the ability to generate surfaces that are both spectrally accurate and morphologically realistic. This hybrid approach provides a versatile tool for reproducing surfaces with identical PSDs and controlled PDFs, suitable for 3D-printing and experimental friction testing—thus bridging the gap between numerical surface generation and physical validation.

4. Experimental setup

This algorithm has made it possible to generate surfaces with both a precise spectral content and a prescribed height distribution defined by skewness and kurtosis. In this way, we can artificially produce surfaces with identical PSDs but different PDFs configurations that do not occur in nature and could not be achieved using conventional methods. This capability is crucial, as it has so far been impossible to assess the independent influence of PDF on the friction coefficient, preventing a clear evaluation of whether spectrum-based and/or distribution-based models are truly reliable.

Table 1
Combination of kurtosis and skewness for generated surfaces.

Kurtosis \ Skewness	0	−1	−2
3	X	X	
5	X	X	X
7		X	X

4.1. Surface generation

Seven surfaces have been generated based on different combinations of kurtosis and skewness, all sharing the same spectral content. The goal was to reproduce surfaces resembling road textures. For this reason, we started from a Gaussian surface with S_{ku} = 3 and S_{sk} = 0, and extended the range up to $S_{ku} = 7$ and $S_{sk} = -2$, values that are typically associated with worn road surfaces. Table 1 shows that the generated surfaces respect the prescribed parameters of kurtosis and skewness.

As shown in the table, the surface with S_{ku} = 3 - S_{sk} = −2 and S_{ku} = 7 - S_{sk} = 0, are not generated for three reasons, the first one is that these seven surfaces are enough to show combined effects, the second is that S_{ku} = 7 - S_{sk} = 0 surface shown a shape very different from something real, with very high-sharp-isolated peaks, the third is

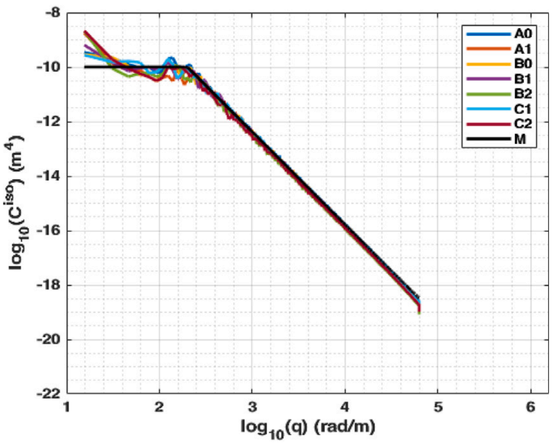

Fig. 3. Seven different radially averaged 2D PSD obtained as output from the seven virtual surfaces using analytical PSD as input (black line - M).

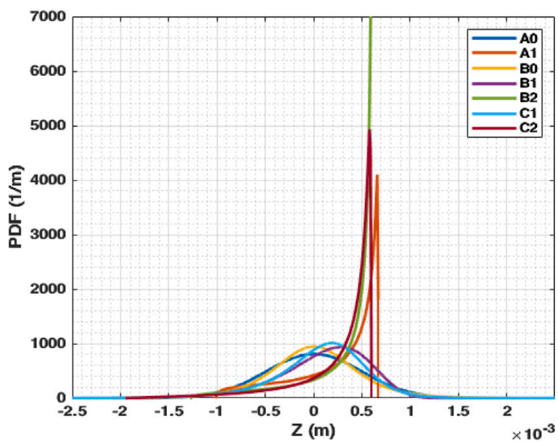

Fig. 4. PDFs obtained as output from the seven virtual surfaces generated via the algorithm.

that the iterative algorithm was not able to create a surface $S_{ku} = 3$ - $S_{sk} = -2$ with low value of kurtosis and high value of absolute skewness.

The surfaces have been generated imposing a specific spectrum and distribution, which are checked after creation. A slight simplification will be explained to make the ranking of the surface easier. For the values of kurtosis *3, 5, and 7*, it will use the letters *A, B, and C*; for the values of skewness *0, −1, −2* it will use the absolute values, obtaining the surfaces *A0, A1, B0, B1, B2, C1, C2*. The spectrum and the distribution are shown respectively in Fig. 3 (Black line - M is the PSD input in the algorithm) and Fig. 4

After the surfaces were generated, several parameters were evaluated to assess their similarity or differences. As shown in Fig. 5, parameters like S_a highlight variations in average roughness among the surfaces, while S_q remains constant. This indicates that all distributions have the same standard deviation, and therefore the same area under the PSD curve [35].

The values of kurtosis and skewness are consistent with the target values. Specifically, the kurtosis matches the expected values up to one decimal place. Skewness values also agree well, except for surface *B2*, which yielded a skewness of −1.65 instead of the desired −2.00. This deviation was accepted because the primary aim of these surfaces is to explore the impact of the height distribution; kurtosis and skewness are simply input parameters used to guide the algorithm.

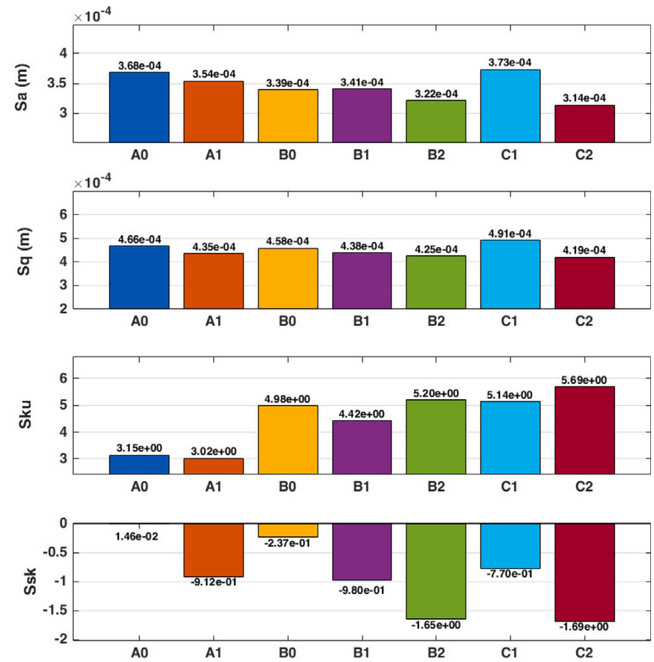

Fig. 5. Roughness parameters obtained as output from the acquisition of the seven surfaces generated via the algorithm.

4.1.1. Surface printing

The following step is the surface 3D printing and the measurement of their topography to check the consistency of the imposed surfaces and the roughness parameters. Other authors have followed this path [44,54], reproducing the spectral properties of rough surfaces but without addressing the statistical distribution of heights. As a result, the generated profiles are implicitly Gaussian, lacking control over non-Gaussian morphologies.

The generated surfaces are realisations of random fields in which both the spectral content (PSD) and the height distribution (PDF) are prescribed. The PSD is imposed through a superposition of harmonic components with random phases, while the PDF is matched using a statistical transformation based on the Johnson family of distributions. This method ensures that the surfaces exhibit random roughness while respecting the target statistical properties. Once the virtual surfaces were generated with the desired spectral and statistical characteristics, they were physically reproduced through 3D printing. This manufacturing step allows us to create realistic, controlled test surfaces for experimental validation. These were printed using a *Form 3* Stereolithography (SLA) printer by *Formlabs*, selected for its high resolution. A material for the surface was *Grey Pro Resin*, a proprietary photopolymer resin developed by *Formlabs*. This resin is specifically designed to provide high precision, good dimensional stability, and balanced mechanical properties suitable for engineering applications. Its main mechanical and thermal properties, measured on post-cured specimens, are summarised in Table 2.

The print path begins to give to the printer the *.stl* file. During printing, light selectively cures a liquid resin to create the shape of the surface. After the deposition of all layers, the parts are removed from the print platform and put in an automated washing in an agitated bath of solvent, eliminating uncured resin for a flawless surface finish. In the end, a curing process with exposure to heat and 405 nm light finalises part properties by completing the chemical reaction started during printing.

The overall dimensions of each printed plate were set to 405×40 mm to fully utilise the Form 3's 150×150 mm build platform: three tiles of 135×40 mm (shown in Fig. 6) were printed simultaneously and then

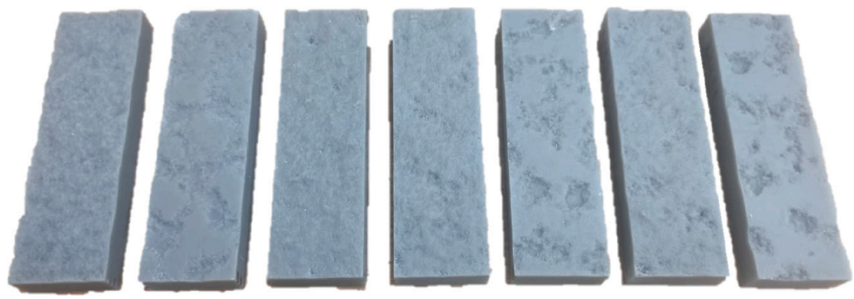

Fig. 6. One tile for each of the seven generated surfaces.

Table 2
Mechanical and thermal properties of Grey pro resin (Formlabs).

Property	Value	Standard
Ultimate tensile strength	61 MPa	ASTM D638
Tensile modulus	2.6 GPa	ASTM D638
Elongation at break	13%	ASTM D638
Flexural stress at 5% strain	86 MPa	ASTM D790
Flexural modulus	2.2 GPa	ASTM D790
Notched Izod impact strength	18.7 J/m	ASTM D256
Heat deflection temperature @1.8 MPa	62.4°C	ASTM D648
Heat deflection temperature @0.45 MPa	77.5°C	ASTM D648
Coefficient of thermal expansion	78.5 μm/m°C	ASTM E831

glued together. This total length also ensured a sufficiently long contact path to explore high sliding velocities without edge effects. Although the printer's native resolution is 25 μm in x, y, and z, we selected a resolution of 50 μm, twice the printer's minimum, in order to satisfy the Nyquist sampling criterion for spatial frequencies while maintaining reasonable build times and part stability. The fidelity of the printed surfaces was then confirmed by re-measuring their topographies. In this way, excessive printing resolution was not used, leading to the printing lasting beyond 24 h without a real benefit on the final result.

4.1.2. Topographic verification of 3D-printed surfaces

The topography measure was performed directly on the tested surfaces. The instrument for the acquisition is a three-dimensional (3D) laser technology based on the principle of triangulation. Although optical topography measurements may present limitations when measuring very steep slopes or highly reflective surfaces [55,56], the present measurements were performed on specimens fabricated using the same resin, manufacturing process and acquisition conditions. Therefore, any systematic measurement bias is expected to be common to all the investigated surfaces and does not affect the comparative analysis carried out in this work. Surface data was processed under ISO 25178-2:2021 [57]. The spectra are obtained following ISO 8608:2016 [58].

Firstly, we checked the correspondence between the surfaces in terms of PSD and PDF. It is crucial that the surfaces exhibit identical spectra and different height distributions between them. It is also important to say that the values of kurtosis and skewness were used only to impose different distributions, and these are not quality-check parameters for the goodness of the printed surfaces.

Fig. 7 shows the PSDs measured from the printed surfaces, compared with the target PSD (black line). All surfaces exhibit excellent agreement with the imposed spectral content across the entire relevant frequency range. This change in slope – from the linear imposed PSD – does not affect the analysis, as all PSDs share the same spectral shape within the range of interest e.i. until $q_1 = 10^6$ m^{-1}. This cut-off is given by [45] corresponding to a short distance cut-off length $d = \pi/q_1 \approx$ 3 μm, which is a typical thickness for the wear layer. Although the nominal printing resolution was 50 μm, the surface topographies were experimentally measured with a lateral resolution allowing the PSD to be evaluated down to wavelengths of approximately 3 μm. Therefore,

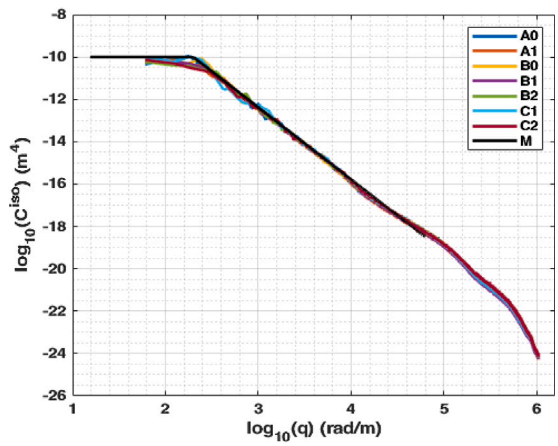

Fig. 7. Radially averaged 2D PSDs measured from the surfaces through the use of a profilometer and imposed analytical PSD (black line - M) to compare the obtained to the imposed.

the spectral content relevant for friction modelling was directly verified on the printed specimens rather than inferred from the printing process. Roughness features below this measurement limit were not experimentally resolved. Although unresolved roughness below the measurement cutoff may contribute to the absolute friction level, it is not expected to significantly affect the relative comparison among the specimens, since all surfaces were manufactured and post-processed under identical conditions. Furthermore, friction models require the use of real PSD without the need to use a linear analytical formulation. This means that although we deviate from having a self-affine surface, the important thing to make the comparison is that the PSDs overlap. The reason for the change in slope is dictated by the fact that as magnification increases, the chemical composition of the resin comes into play in the roughness.

Fig. 8 exhibits how the surfaces have different height distributions with good uniformity between all the surfaces.

This procedure produced seven distinct surfaces that share virtually identical PSDs, so much so that their PSD curves overlap almost perfectly and are indistinguishable, while exhibiting a wide range of height distributions (PDFs).

To probe the decisive role of surface morphology beyond the PSD, we therefore carried out a comprehensive test campaign on a high-speed linear friction tester, measuring total and lubricated friction for each surface and thus delineating the limits of the PSD to describe rubber friction.

4.2. High speed linear friction tester

Friction rigs, how the Linear Friction Testers (LFT) have been used since the time of Leonardo Da Vinci [59] due to their capability to

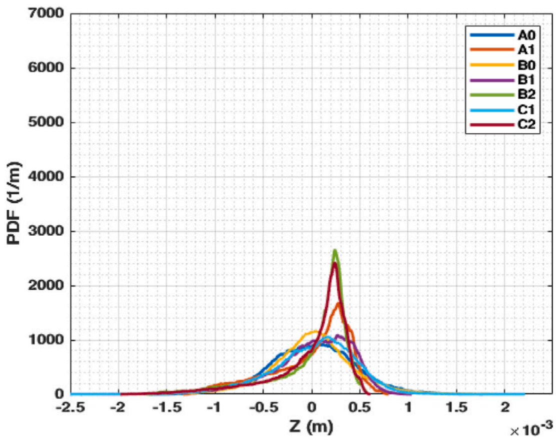

Fig. 8. PDFs measured from the acquisition of the surfaces.

perform the test under controlled boundary conditions. Obviously, technology evolved over time, leading to having very efficient LFT able to make tests over rigid boundary conditions in terms of, sliding velocity, temperature, and contact pressures [60].

The boundary conditions adopted in this work were selected to ensure stable and comparable measurements across the different surfaces. The chosen pressure and velocity ranges are representative of typical tribological tests on rubber materials and allow differences arising from surface morphology to emerge clearly. Moreover, the combination of dry and lubricated conditions provides a practical way to suppress adhesion and highlight the role of hysteretic deformation.

To perform these measurements, we used the High-Speed Linear Friction Tester (HiLiTe) [61], shown in Fig. 9, an apparatus specifically designed to reproduce controlled sliding conditions representative of tyre–road interaction at laboratory scale.

The relative positioning of the surfaces with the sliding path is ensured by gluing them on a steel plate with the use of a jig to respect the distances by the edge of the plate. The gluing process is shown in Fig. 10.

Two printed surfaces were mounted side-by-side on a single steel plate. After completing tests on the first tile, we simply rotated the entire plate by 180°, rather than re-aligning it, to bring the second tile into the sliding path, thereby preserving the exact relative positioning between the rubber specimen and the surface under test (Fig. 9).

A different jig was used to centre the sample on the steel plate, as shown in Fig. 11.

To avoid adhesion during sliding, Grosch proposed using magnesia powder [62], but this approach was primarily applied to sandpaper or glass. Using powders on rough surfaces may alter the topography itself, since the particles can clog micro-cavities. In contrast, a thin silicone oil film (3 cSt) and the flat-on-flat configuration avoid the crack opening process and thus suppress the molecular rubber-substrate adhesion [63], without modifying the surface roughness. In this configuration, hysteretic deformation is preserved, while the adhesive contribution is eliminated. Nevertheless, it must be noted that the confined oil within the real contact regions may still undergo shear, introducing a minor viscous contribution. Therefore, the lubricated condition should be regarded as an effective way to suppress adhesion, while the measured friction may include both hysteretic and a small viscous component [64]. The respective components will be called μ_{hyst} for the hysteretic part and μ_{cont} for the part without hysteresis.

Fixed all the boundary conditions and the requirements; the test path consists of the samples run-in and into the measures. Every sample is required to be conditioned on the appropriate surface where it will slide, for several repetitions, until the friction coefficient is stable and the surface loses its surface patina; the number of repetitions depends on the reference surface. The sliding velocity is maintained at $1\ \text{m/s}$, and the contact pressure is set appropriately for the measurement.

Knowing the working range of the rig, a test matrix was chosen to investigate the influence of road descriptors on friction in a controlled environment while varying those strategies for highlighting specific phenomena, particularly saturation effects and the influence of sliding speed on the contact area and friction.

5. Test plan & Procedure

This section describes the experimental activities performed to evaluate the effect of surface morphology on rubber friction. The following paragraphs present the testing procedure adopted for all trials and the specific operating conditions, including load, velocity, temperature, and lubrication state.

The rubber specimen was mounted beneath two load cells. This configuration was adopted to ensure measurement redundancy and to compensate for possible pitch or roll moments during the contact phase, thus providing a more stable and accurate assessment of both normal and tangential forces throughout the sliding path.

During each test, the specimen was first accelerated to the target velocity, while the incoming temperature was recorded by an infrared pyrometer. The sample was then gradually lowered onto the test surface through a controlled ramp, ensuring a smooth engagement and minimising dynamic transients at contact initiation. The sliding stroke covered approximately 200 mm under constant nominal load. At the end of the track, a second ramp lifted the specimen progressively, preventing impact or shock at exit. The outgoing temperature was again measured by the pyrometer to quantify the thermal rise during the sliding motion. Each test sequence consisted of five consecutive runs under identical conditions (except the velocity), followed by surface cleaning to remove rubber residues.

To comprehensively characterise the frictional behaviour, the tests were carried out under controlled conditions, varying key parameters related to the material, load, sliding speed, and lubrication state, as detailed below.

- **Compound and Size Selection:** Each specimen had a square area of 900 mm^2 and two model rubber compounds, based on carbon black, natural rubber, and emulsion-polymerised styrene-butadiene rubber (ESBR), were specifically designed for this study to exhibit distinct viscoelastic modulus and hysteresis characteristics.
  Fig. 12 shows the viscoelastic characteristics of compounds A and B in terms of storage modulus (G') and loss factor ($\tan\delta$), obtained from temperature sweep tests performed with a Metravib DMA+1000 in shear mode at a frequency of 10 Hz with a dynamic strain of 0.1%. All the shown results are dimensionless with respect to the maximum value of the storage modulus (a) and the loss factor (b) of the compound A.
  Compound B exhibits both a higher storage modulus and a higher loss factor compared to compound A. This indicates that compound B is simultaneously stiffer and more dissipative. Specifically, the higher storage modulus implies that compound B can store a greater amount of elastic energy during deformation, offering greater resistance to strain and exhibiting a more elastic and structurally solid behaviour than compound A. At the same time, the higher loss factor of compound B means that a larger fraction of the absorbed energy is dissipated as heat, resulting in an enhanced ability to dampen vibrations, impacts, or cyclic loads.
- **Nominal Contact Pressures:** Tests were conducted at two different nominal contact pressures (0.15 MPa and 0.30 MPa) to analyse the contribution of the various surfaces to the real contact area saturation.

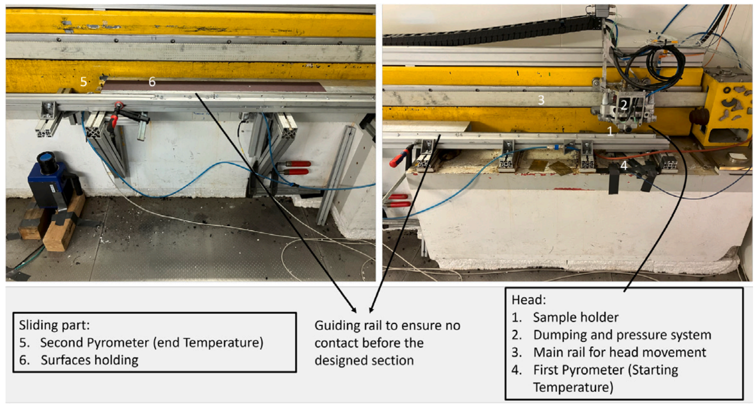

Fig. 9. High Speed Linear Friction Tester (HiLiTe) of Leibniz University of Hannover and its equipment.

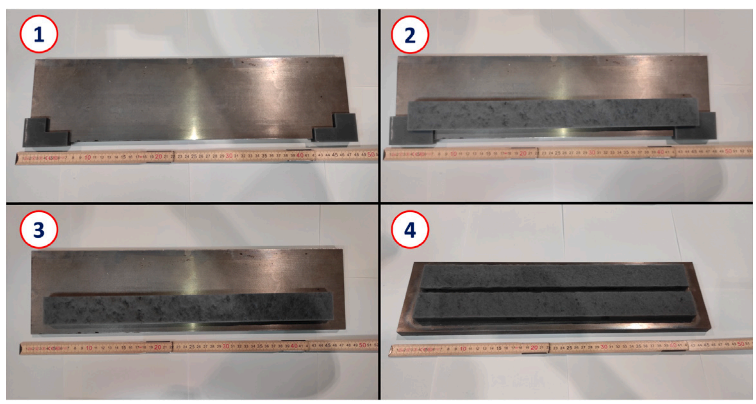

Fig. 10. Procedure for gluing surfaces: (1) Jig positioning; (2) Gluing surfaces; (3) Jig remotion; (4) Final result.

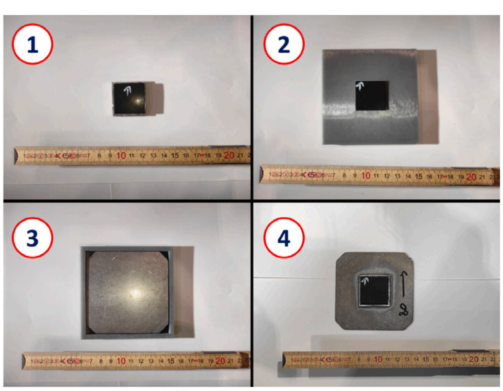

Fig. 11. Procedure for gluing samples: (1) Rubber sample on first steel plate; (2) Jig positioning (front); (3) Jig positioning (rear); (4) Final result.

- **Temperature:** The temperature was fixed at 30°C. This value was chosen to minimise variations due to the thermal behaviour of the compound, as the main focus of the study is not to delve into the temperature dependence of friction but rather to concentrate on the effects of road descriptors and contact conditions.
- **Sliding Speed:** The experimental matrix includes tests at seven different speeds (0.01, 0.03, 0.1, 0.3, 1, 2, and 5 m/s). This selection is based on theoretical and empirical models, which highlight how the contact area and the deformation mechanisms (thus, friction generation) are strongly dependent on the sliding speed.
- **Surface Conditions: Dry and Lubricated:** Tests were performed in two modes: under dry conditions and under lubricated conditions. The use of lubrication allows the elimination of the adhesive (or "sticky") component of the contact. By subtracting the contribution from the lubricated tests from the total friction, it is possible to isolate and analyse the actual adhesive portion.

Tests were conducted at different sliding speeds ranging from 0.01 m/s to 5 m/s. As expected, such conditions led to a certain degree of frictional heating. Nevertheless, the temperature rise was found to be very similar across all the investigated surfaces. The maximum deviation between the seven road samples did not exceed 15°C at 5 m/s. Although the heating effect becomes more pronounced at the highest sliding speeds, its magnitude was essentially consistent across all surfaces. Therefore, the results can be considered comparable, and the analysis remains focused on the influence of road surface roughness on frictional behaviour. Five repetitions were done for each condition. A new rubber sample was used every time the testing conditions and surfaces changed (except for the different velocities). For the lubricated test, all samples were conditioned together on dry surfaces and underwent five preparatory strokes under the same load and speed to fully recondition the rubber on the lubricated surface immediately before taking measurements.

Summarising the test matrix, the experiments covered seven 3D-printed surfaces, two surface conditions, two rubber compounds, two

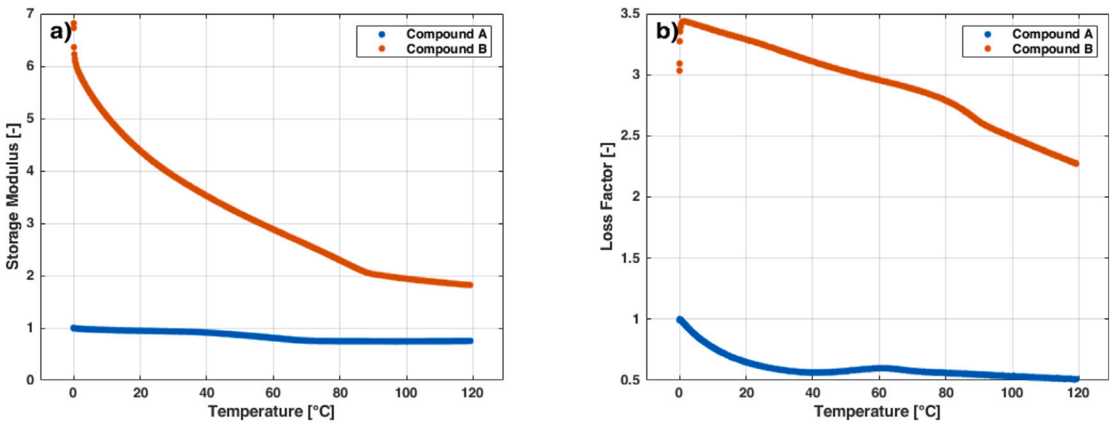

Fig. 12. Viscoelastic properties of compounds A and B: storage modulus G' (a) and loss factor $\tan\delta$ (b) as a function of temperature, measured in shear mode at 10 Hz with a dynamic strain of 0.1%.

nominal contact pressures, and seven sliding velocities. This combination results in a total of 392 unique testing conditions. Considering the five repetitions performed for each condition, a total of 1960 individual friction measurements were collected during the campaign.

Following the tests, we considered that a comparison of the results with spectrum-based models could be of great interest and could lend greater significance to the tests themselves.

6. Results & Discussion

The following sections present the results obtained for each set of surfaces, exploring how surface morphology, lubricant, load, and velocity influence the overall frictional response. These complementary perspectives enable us to better understand the combined role of surface descriptors and contact mechanics in governing rubber–surface interaction before taking measurements.

6.1. *Theoretical prediction & Simulation*

To perform a meaningful comparison with theory, Persson's model was implemented using the experimentally measured PSD and the viscoelastic properties of the tested compounds as input. Since spectrum-based models require calibration of the contact-related (adhesive) contribution through fitting procedures, a reference condition was selected.

The Gaussian surface A0 was chosen as the reference surface for calibration. This choice is motivated by the fact that classical contact and friction theories are typically formulated under the assumption of Gaussian roughness. Therefore, A0 represents the most theoretically consistent case for establishing a baseline comparison between experimental data and model predictions.

In Persson's framework, the adhesive (or contact-related) contribution to friction is introduced through a phenomenological interfacial shear strength $\tau_f(v)$, which depends on sliding velocity. The adhesive friction coefficient can be expressed as:

$$\mu_{\mathrm{adh}} = \frac{\tau_f(v)}{\sigma_0}\frac{A_c}{A_0} \tag{5}$$

where σ_0 is the nominal contact pressure and A_c/A_0 is the real-to-nominal contact area ratio predicted by the contact mechanics formulation discussed above.

The velocity-dependent shear strength $\tau_f(v)$ is commonly described using a log-Gaussian (Gaussian-like in $\ln v$) phenomenological expression:

$$\tau_f(v) = \tau_{f0}\exp\left[-c\left(\ln\frac{v}{v_c}\right)^2\right] \tag{6}$$

where:

Table 3
Fitting parameters of the adhesive term identified on the Gaussian reference surface (A0).

Compound	τ_{f0} [MPa]	c	v_c [m/s]
A	3.409	0.165	0.007
B	3.225	0.154	0.012

- τ_{f0} is the maximum interfacial shear strength,
- v_c is the characteristic velocity at which the adhesive contribution reaches its peak,
- c is a parameter controlling the width of the Gaussian curve in logarithmic velocity space.

This formulation is consistent with the classical bell-shaped dependence of friction on sliding velocity observed experimentally (e.g. Grosch-type behaviour), and follows the same principles of time–temperature superposition typically used in rubber friction analysis.

In the present work, the fitting parameters τ_{f0}, v_c, and c were identified using the experimental friction data obtained on the Gaussian reference surface (A0). It should be noted that the present implementation inherits the assumptions of the original spectrum-based formulation. In particular, the viscoelastic response is described through the measured linear viscoelastic properties of the compounds and does not explicitly account for thermo-mechanical phenomena such as frictional heating or flash-temperature effects. Consequently, the comparison is intended to assess the capability of the model to reproduce the relative influence of surface morphology rather than to provide a fully quantitative prediction of friction over the entire velocity range. Once calibrated, the same model formulation and fitted parameters were retained when evaluating the remaining non-Gaussian surfaces, without any further adjustment. In this way, any deviation between model predictions and experimental measurements for the non-Gaussian surfaces can be directly attributed to the influence of the height distribution (PDF), which is not explicitly accounted for in the current spectrum-based theoretical framework. The resulting model predictions are shown in Fig. 13.

The fitting parameters used in the adhesive contribution are reported in Table 3. These parameters were identified using the experimental data of the Gaussian reference surface (A0) at low pressure and subsequently kept constant for all other surfaces and operating conditions.

Fig. 13 shows the model predictions obtained for all seven surfaces within the same sliding velocity and load ranges explored experimentally. It can be observed that the model returns almost overlapping friction curves for all surfaces, with only minor separations in specific

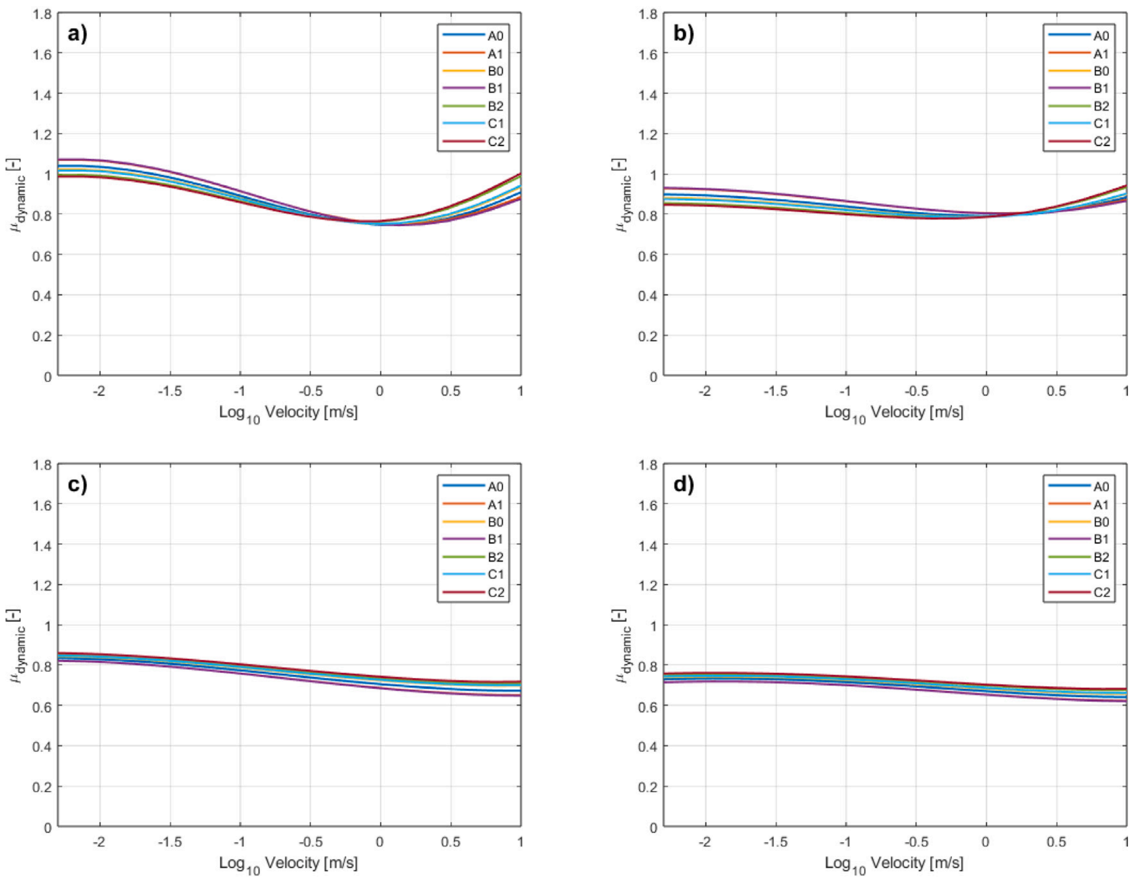

Fig. 13. Model predictions according to Persson's theory against base-ten logarithm of velocity at the two nominal contact pressures 0.15 MPa (a & c) and 0.30 MPa (b & d) and two different compounds, A (a & b) and B (c & d), for each surface (different colours), using fixed fitting parameters and varying the measured PSDs of the generated surfaces.

conditions. In particular, whenever a ranking between surfaces appears, it does not correspond to the ranking observed experimentally.

For compound A, a slight categorisation of the curves can be noticed at lower sliding velocities. This behaviour is likely related to its lower storage modulus E', which makes the material more sensitive to variations in the real-to-nominal contact area ratio A_c/A_0 predicted by the model. However, no pronounced separation between the two nominal contact pressures is observed, even though the friction level is consistently lower at the higher load, as expected from contact saturation effects.

In contrast, compound B exhibits almost indistinguishable friction curves across the different surfaces. The predicted friction levels are overall lower at the higher nominal pressure, but the separation between surfaces is minimal. This reflects the reduced sensitivity of the stiffer compound to small variations in the predicted contact area, leading to nearly identical model responses for all PSD-identical surfaces.

6.2. Overall dry measure and the role of the surfaces

The overall results are presented as the friction coefficient plotted against the sliding velocity on a base-ten logarithmic scale, in line with the format typically used in the theoretical models [3,20]. Each friction value visible in the plots (circular markers) corresponds to a friction measurement. The experimental data were approximated using a smoothing spline, defined as the function that minimises a combination of the squared approximation error and the spline curvature, thus producing a smooth curve consistent with the overall data trend. These have been added to make the differences between the various surfaces more easily visible.

To further assess the consistency between model and experiments, the previous model predictions (shown in black) are superimposed onto the experimental friction data in Fig. 14. It can be observed that, particularly for compound B, the fitted model curve closely follows the experimental points of the Gaussian reference surface A0, confirming the internal consistency of the fitting procedure. However, deviations become evident for the non-Gaussian surfaces, indicating that differences observed experimentally cannot be captured by spectral information alone.

Fig. 14 shows the measurements performed on dry surfaces for two contact pressures and seven different sliding velocities. Each colour in the legend represents a different surface.

As found in literature, velocity affects the viscoelastic response of rubber, influencing friction. Therefore, analysing its effect across all surfaces provides insights into how morphology interacts with rate-dependent energy dissipation. As shown in Fig. 14, for each surface the friction coefficient generally decreases with increasing velocity. This observation is perfectly in line with the findings of Grosch [62] on sandpaper, as well as with later studies on concrete and asphalt surfaces [36,45], and is therefore confirmed also on resin-printed surfaces.

Regarding load effects, contact theories based on the surface power spectrum describe saturation phenomena as being governed by the spectral content of roughness [4,65]. Within these frameworks, the saturation behaviour is formulated as a function of the frequency distribution of surface asperities, while the explicit role of height distribution is not accounted for. Consequently, when interpreted strictly within the assumptions of these models, surfaces sharing the same PSD are expected to exhibit similar trends in friction reduction with increasing nominal pressure.

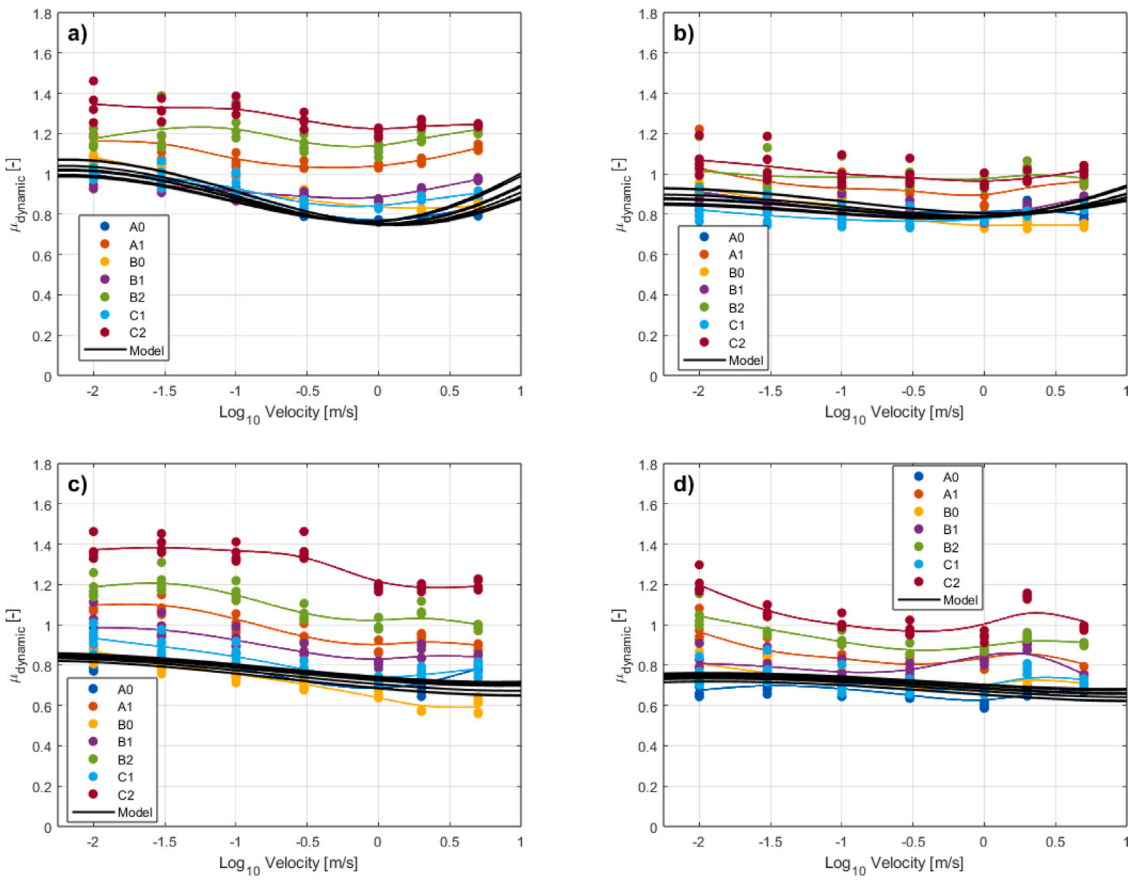

Fig. 14. Persson model predictions (black curves), calibrated on surface A0, superimposed on the Total dry friction against base-ten logarithm of velocity at the two nominal contact pressures 0.15 MPa (a & c) and 0.30 MPa (b & d) and two different compounds, A (a & b) and B (c & d) for each surface (different colours).

Despite sharing identical PSDs, the measured friction coefficients differ among the surfaces, indicating that additional roughness descriptors play a role. The ranking of the surfaces for the two conditions of nominal contact pressure for the compound B is *C2, B2, A1, B1, C1, A0, B0*. Instead, for *0.30* MPa, there is an inversion between *A0, B0*, The same it is not possible to be said for compound A, which maintains the same ranking for surfaces C2, B2, and A1, while the other surfaces show crossovers at different speeds, indicating that speed has a strong influence on friction beyond simple roughness effects. At the nominal pressure of 0.30 MPa, however is evident that there is an overall decrease in the friction coefficient, but no significant differences between the surfaces can be observed, although it remains evident that for both compounds, the friction coefficients differ between various surfaces across the two nominal contact pressures, despite identical PSDs, highlights that additional descriptors beyond the PSD – such as the height distribution (PDF) and related roughness parameters – also contribute to the frictional response and may help explain the differences observed among the surfaces.

To further emphasise the relative differences among the surfaces, the total dry friction coefficients were normalised with respect to the Gaussian reference surface (A0). This representation allows a direct comparison of how each non-Gaussian surface deviates from the Gaussian case under identical testing conditions (Fig. 15).

For each compound and nominal pressure, the friction values at a given sliding velocity were normalised with respect to the Gaussian reference surface (A0). At each velocity, the mean of the five A0 repetitions was used as a reference, and all corresponding values were divided by it. As a result, A0 appears as a constant line equal to 1, while the other surfaces directly express their relative deviation from the Gaussian reference.

Fig. 15 shows that the normalised friction response exhibits a strongly non-uniform dependence on the height distribution across operating conditions. For selected surface–compound–pressure combinations, the curves closely follow the Gaussian reference (A0), whereas pronounced deviations occur in other cases, particularly at specific sliding velocities.

Under dry conditions, non-Gaussian surfaces can produce relative differences of up to approximately 80% with respect to the Gaussian baseline. This confirms that, despite identical PSDs by construction, the statistical height distribution alone can significantly affect the contact-related contribution to friction within specific loading and velocity regimes.

6.3. Avoiding adhesion

Fig. 16 presents the friction results obtained under lubricated conditions. In contrast to the dry case, no systematic ranking among surfaces is observed, neither at low nor at high nominal pressure, and the overall velocity dependence differs markedly from that reported in Fig. 14.

In the present work, lubrication was adopted as an experimental strategy to strongly reduce the contact-related contribution to friction, allowing the hysteretic component to become dominant. It should, however, be emphasised that this approach represents an approximation rather than a complete physical separation of the friction mechanisms. Depending on the operating conditions, partial squeeze-out of the lubricant may occur at low sliding speeds, while hydrodynamic lift may develop at higher speeds. Furthermore, adhesive friction is known to include molecular bonding mechanisms in addition to crack-opening processes. Consequently, the lubricated measurements should be interpreted as hysteresis-dominated conditions rather than as purely

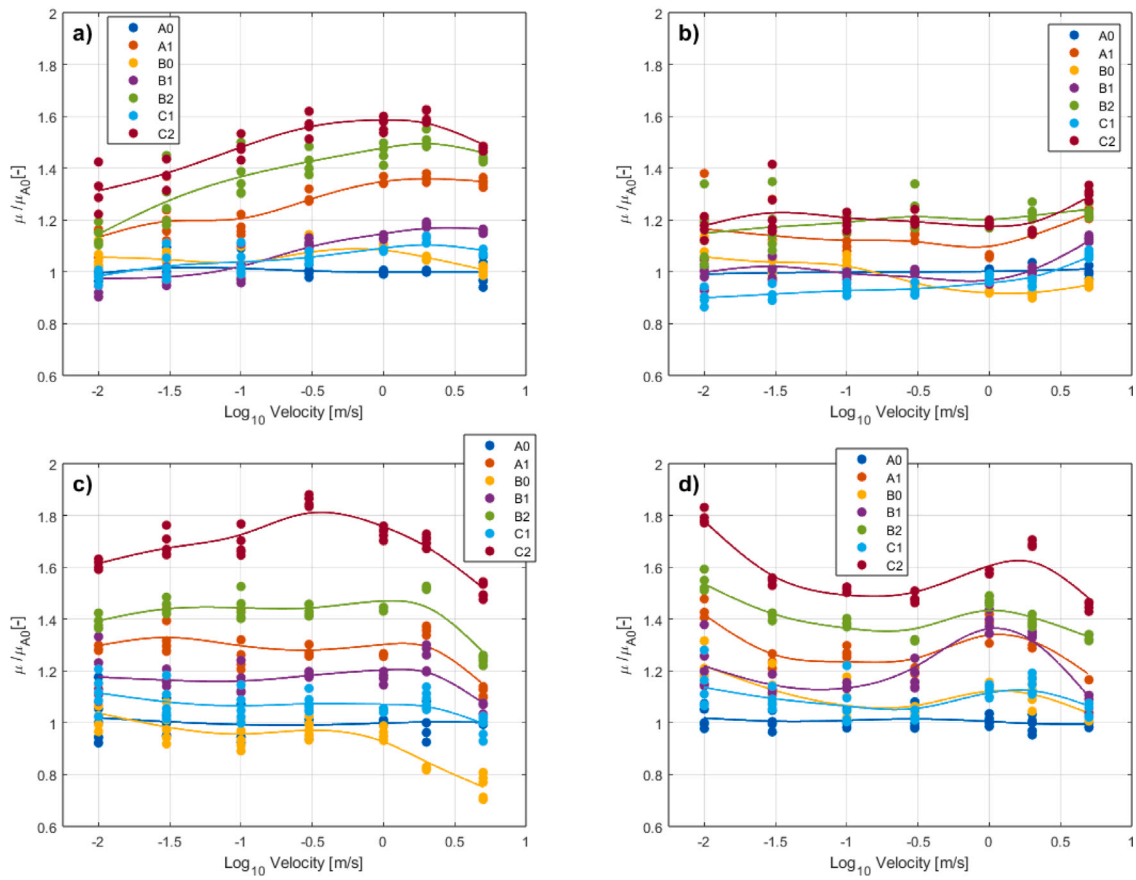

Fig. 15. Normalised total dry friction coefficient with respect to the Gaussian reference surface A0 at the two nominal contact pressures 0.15 MPa (a & c) and 0.30 MPa (b & d), and for the two rubber compounds, A (a & b) and B (c & d). Each colour represents a different surface.

hysteretic friction. Nevertheless, since all the investigated surfaces were tested using the same lubricant, under identical operating conditions and following the same experimental procedure, this approximation does not affect the comparative analysis carried out in the present work.

The experimental data exhibit a much closer agreement with spectrum-based model predictions, with friction coefficients that nearly overlap across all surfaces and follow a common trend. The maximum spread between minimum and maximum values is limited to 0.083 at low pressure and 0.094 at high pressure. These observations indicate that, once the contact-related contribution is substantially reduced, the remaining friction becomes much less sensitive to the imposed height distribution and is predominantly governed by the surface spectral content (PSD). Such qualitative behaviour is consistent with existing conceptual frameworks for smooth and weakly rough surfaces, where viscoelastic dissipation becomes the dominant mechanism, although a comprehensive theoretical formulation of the contact-related contribution is still lacking [24,64].

To enable a direct comparison with the dry condition, the same normalisation procedure adopted in Fig. 15 was applied to the lubricated data. For each sliding velocity, friction coefficients were normalised by the mean value measured on the Gaussian reference surface (A0) under identical compound and nominal pressure.

Fig. 17 reports the corresponding normalised friction coefficients. A clear difference with respect to the dry condition emerges: under lubricated conditions, relative deviations among surfaces are substantially reduced. In most cases, the normalised values remain within 20% of the Gaussian reference, with only sporadic excursions approaching approximately 30% at isolated velocities.

Unlike the dry case—where deviations reached significantly larger magnitudes—these variations do not exhibit any systematic dependence on the imposed height distribution. Instead, the curves cluster closely around unity, indicating that once the contact-related contribution is substantially reduced under lubricated conditions, the influence of the height PDF becomes marginal.

These results confirm that the hysteretic component of friction is predominantly governed by the spectral content (PSD), whereas the height distribution primarily affects the contact-related contribution observed under dry conditions. The lubricated measurements therefore reinforce the interpretation that the PDF influences total friction mainly through its effect on real contact mechanics rather than on viscoelastic dissipation.

The “no hysteretic” part of friction [45] is obtained by subtracting the hysteretic contribution from the total friction coefficient [62] (see Fig. 18).

Subtraction of the hysteretic part does not change the ranking seen in the total friction coefficient; this confirms that the differences in the hysteretic component are negligible and that the PSD is indeed the dominant descriptor for hysteresis-driven friction. Consequently, the variations observed in the total coefficient must primarily originate from the contact-related contribution, which is sensitive to the statistical height distribution. This distinction not only highlights the importance of separating hysteretic and contact contributions but also provides the basis to explore how other factors, such as the applied load, further influence the frictional response. The same experimental dataset, therefore, allows us to assess how increasing the nominal pressure modifies the friction coefficient, offering additional insights into the mechanisms governing rubber–road interaction.

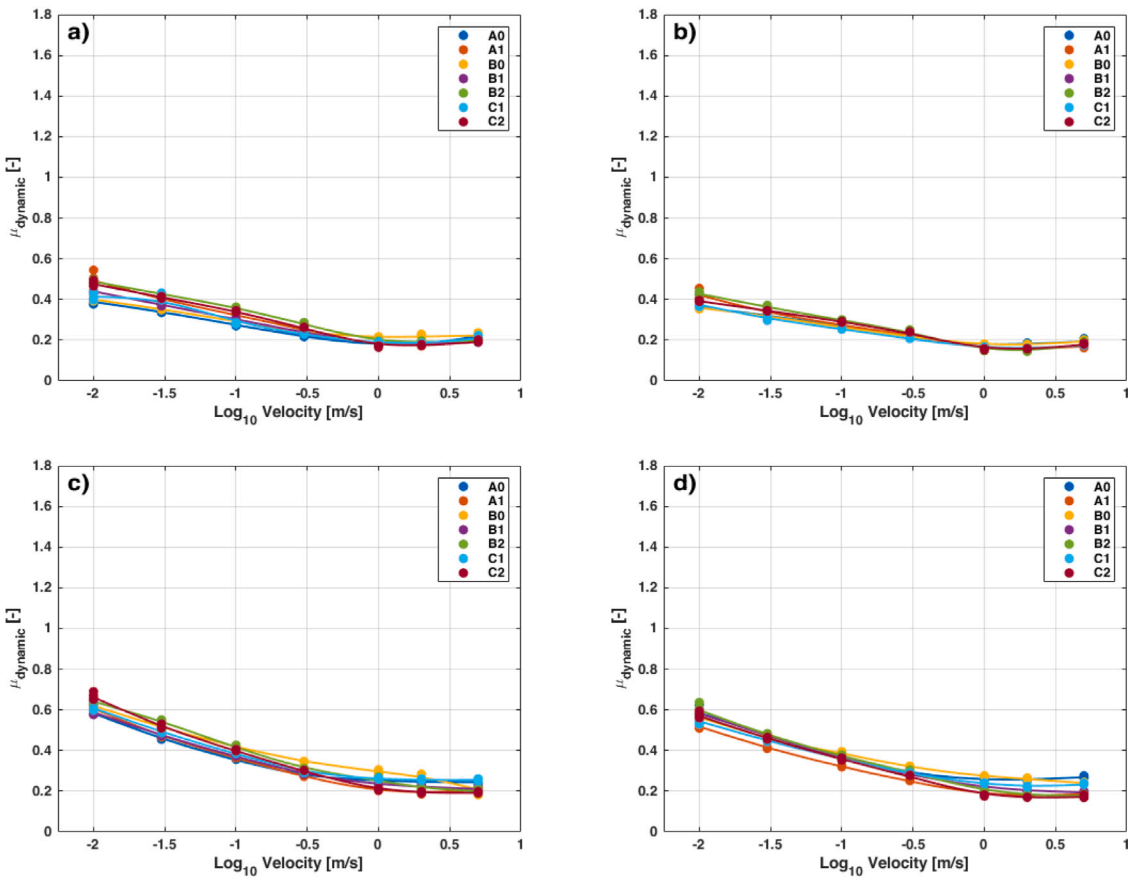

Fig. 16. Friction measured under lubricated condition against base-ten logarithm of velocity at the two nominal contact pressures 0.15 MPa (a & c) and 0.30 MPa (b & d) and two different compounds, A (a & b) and B (c & d) for each surface (different colours).

Having experimentally reduced the contact-related contribution through the lubricated tests, the next step is to investigate how changes in mechanical loading affect the friction coefficient. The nominal pressure, in particular, governs the extent of real contact and provides key insights into the saturation behaviour of rubber–road interfaces.

6.4. *The role of the load*

Another important aspect that can be analysed from these measurements is the effect of increasing the load on the friction coefficient. In this context, increasing the load corresponds to increasing the nominal pressure, which in these experiments was set to 0.15 MPa and 0.30 MPa.

It is well established that, in rubber–surface friction, a saturation effect of the maximum transferable traction force occurs, leading to a decrease in the friction coefficient. This phenomenon is observed both at the tyre scale [66] and at the scale of a single rubber block in contact with a generic rough surface [4,65]. The physical origin of this behaviour lies in the fact that, as the load increases, the real contact area also increases, but in a non-linear proportion with respect to the nominal load.

However, the experimental results show a different picture, as illustrated in Fig. 19. In these plots, the vertical axis reports the decrease of the friction coefficient, while the horizontal axis shows the seven generated surfaces. For each surface, results are presented for the three sliding speeds (lowest, middle, and highest). Previously, friction values were shown for each measurement; now each bar corresponds to the decrease calculated from the median of the five values for each condition (this statement applies to all subsequent bar plots).

As shown in Fig. 19, under dry conditions, the reduction in the friction coefficient with increasing nominal pressure varies significantly across the tested surfaces, revealing the influence of height distribution and surface morphology on contact saturation. The effect is particularly pronounced for surfaces C1 and C2, which exhibit the largest decrease in friction. In contrast, under lubricated conditions, $\Delta\mu$ values are minimal and almost identical for all surfaces, confirming that the hysteretic component remains primarily controlled by the PSD.

6.5. *The role of compound*

As mentioned in Section 5, two rubber compounds were tested, differing in viscoelastic moduli and hysteretic characteristics. It is evident from Fig. 12 that compound B exhibits both a higher storage modulus and a higher loss factor compared to material A. Therefore, we can state that compound B is overall stiffer and more dissipative. In other words, material B offers greater resistance to elastic deformation—showing a more solid-like structure—while also dissipating a larger portion of energy as heat, thus providing improved damping of vibrations and cyclic stresses.

From these considerations, it can be inferred that material B is expected to exhibit a higher hysteretic friction component than material A, while the opposite should hold for the non-hysteretic or total friction.

The graphs compare the friction coefficients of the two compounds, focusing on only three reference sliding velocities—low, intermediate, and high—to avoid overloading the discussion.

In Fig. 20, plots show the differences in terms of friction between the compounds for both the nominal contact pressure and three velocities. At both low and high sliding speeds, compound A consistently exhibits

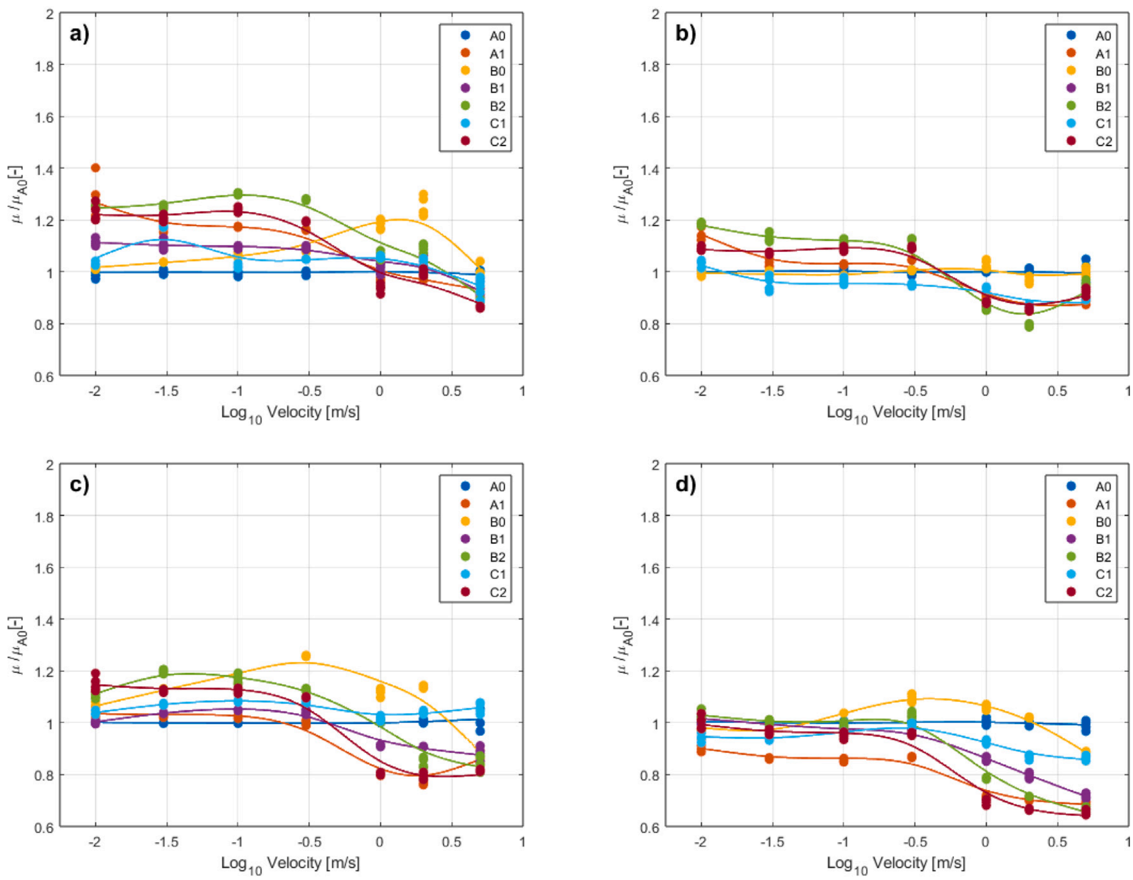

Fig. 17. Normalised lubricated friction coefficient with respect to the Gaussian reference surface A0, plotted against base-ten logarithm of velocity at the two nominal contact pressures 0.15 MPa (a & c) and 0.30 MPa (b & d) and for the two compounds A (a & b) and B (c & d).

higher friction coefficients than compound B. Despite identical spectral content, the seven printed surfaces show measurable differences in friction, demonstrating the role of surface morphology beyond the PSD. The overall decrease in friction with increasing speed aligns with the literature.

A very different trend is observed under lubricated conditions, shown in Fig. 21, which highlights only the hysteretic characteristics of the materials. As expected, the results are inverted compared to the dry tests: compound B now exhibits higher hysteretic friction than compound A. Under lubricated conditions, the friction coefficients are significantly lower than in dry contact, confirming the effective suppression of adhesive interactions. The results show no clear ranking among the surfaces, indicating that when adhesion is excluded, the PSD is the dominant descriptor governing hysteretic friction. Compound B consistently exhibits slightly higher friction values than compound A, consistent with its higher loss factor and energy dissipation capability. The increase in nominal pressure from 0.15 MPa to 0.30 MPa causes a modest overall reduction in friction, reflecting the expected saturation effect at higher loads.

An opposite behaviour is found for the non-hysteretic friction results, shown in Fig. 22. These findings are consistent with the viscoelastic characterisation of the two compounds: The stiffer and more dissipative compound B shows higher hysteretic friction, while compound A- softer and less damped- exhibits higher total and contact friction. This confirms that the compound's viscoelastic response modulates the relative contribution of hysteretic and contact components, even when the surface characteristics remain unchanged.

Overall, the comparison between the two compounds confirms that the relative magnitude of hysteretic and contact contributions depends on the viscoelastic modulus and damping capacity of the material, consistently with their DMA characterisation.

A key outcome is that, for the same increase in nominal pressure (0.15→0.30 MPa), the *reduction* in friction is not universal across surfaces sharing the same PSD: it depends on the specific morphology (PDF) and on the rubber compound. In some cases the drop is larger for compound B than for A (e.g., surface A0, Fig. 23, a), in others the opposite holds (e.g., surface B0, Fig. 23, b), while for certain surfaces, the decrease is comparable for both compounds (e.g., surface C1, Fig. 23, c). This surface–compound interplay persists across the three reference speeds considered, even though the absolute magnitude of the reduction may vary. Hence, the load sensitivity of friction cannot be ascribed to spectral content alone: it emerges from the combined effect of surface height distribution and the viscoelastic response of the material.

The experimental results discussed in these sections showed that surfaces sharing identical PSDs may nevertheless exhibit significantly different dry-friction behaviour. In particular, the observed differences in friction saturation with increasing load suggest that the mechanisms governing the evolution of the real contact area may not be fully described by the spectral content alone. Since the contact-related contribution is expected to dominate dry friction conditions, this observation led to the hypothesis that differences in the statistical height distribution (PDF) could induce different contact formation and contact saturation mechanisms, even for surfaces characterised by the same PSD.

To qualitatively investigate this hypothesis, a numerical contact-mechanics analysis based on a Boundary Element Method (BEM) was

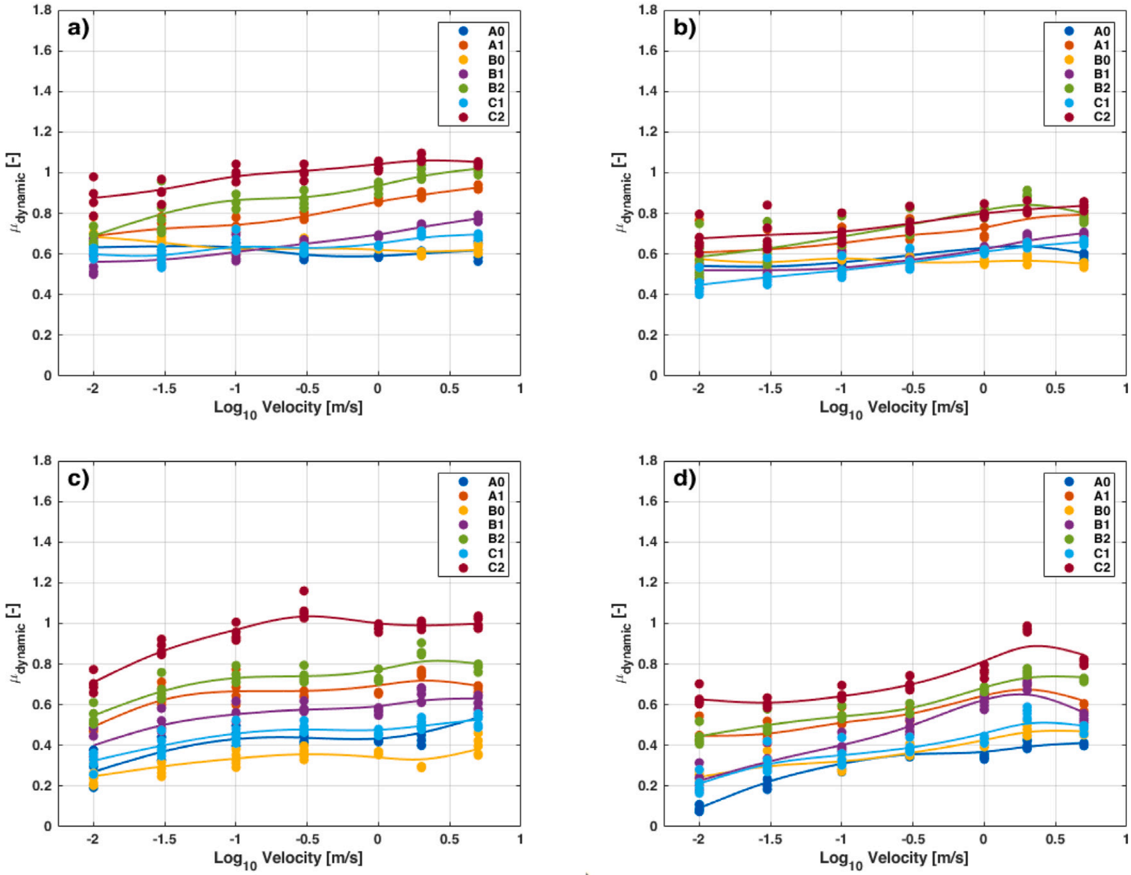

Fig. 18. No-hysteresis friction against base-ten logarithm of velocity at the two nominal contact pressures 0.15 MPa (a & c) and 0.30 MPa (b & d) and two different compounds, A (a & b) and B (c & d) for each surface (different colours).

introduced. The objective of this analysis is not the quantitative prediction of friction coefficients, but rather the verification of whether surfaces sharing the same spectral content but different PDFs may exhibit different evolutions of the real contact area under load. Although the adopted numerical framework relies on simplified assumptions, such as linear elasticity and frictionless normal contact, it provides a physically meaningful tool to qualitatively assess whether the experimentally observed friction trends are consistent with differences in contact-area evolution induced by the surface height distribution.

7. Theoretical interpretation and qualitative consistency of experimental results

The experimental results presented in the previous sections demonstrate that surfaces sharing the same PSD may nevertheless exhibit markedly different dry-friction responses. This observation raises an important question regarding the origin of these differences and whether they can be reconciled with current spectrum-based friction theories. To address this point, the following analyses progressively examine the problem from three complementary perspectives: first, through the use of the Top PSD within Persson's theoretical framework; second, through numerical contact-mechanics simulations based on the Boundary Element Method (BEM); and finally through direct experimental measurements of the contact area.

7.1. Top PSD-based interpretation

The conventional PSD describes the spectral content of the entire surface topography, independently of whether all height levels are effectively involved in the rubber–surface interaction. Under finite loading conditions, however, the rubber does not completely penetrate the roughness profile and contact is initially established through the highest asperities. For this reason, the *Top PSD*, obtained by retaining only the portion of the topography located above the mean plane, has been proposed as an approximate spectral representation of the surface region more likely to participate in contact [4,44].

It should be emphasised that the Top PSD does not provide an exact representation of the roughness effectively experienced by the rubber, since the actual penetration depth depends on load, compound properties, sliding velocity, and temperature. Nevertheless, it provides a useful intermediate descriptor for investigating whether the upper portion of surfaces sharing the same complete PSD contains sufficient morphological information to distinguish their frictional responses.

The radially averaged Top PSDs calculated for the seven printed surfaces are reported in Fig. 24. Unlike the complete PSDs, which are virtually indistinguishable, the Top PSDs exhibit a clear and systematic separation.

Considering their overall spectral level, the Top PSDs approximately follow the decreasing order

$B0,\ A0,\ C1,\ B1,\ A1,\ B2,\ C2.$

This ranking indicates that the upper portions of the surfaces retain markedly different spectral characteristics, despite the complete PSDs being identical by construction. In particular, surfaces such as B0 and A0 exhibit comparatively higher Top PSD levels, whereas B2 and C2 exhibit the lowest values over most of the investigated wavevector range.

To evaluate the consequences of these differences within a spectrum-based friction framework, Persson's model was subsequently recalculated using the measured Top PSD of each surface as spectral

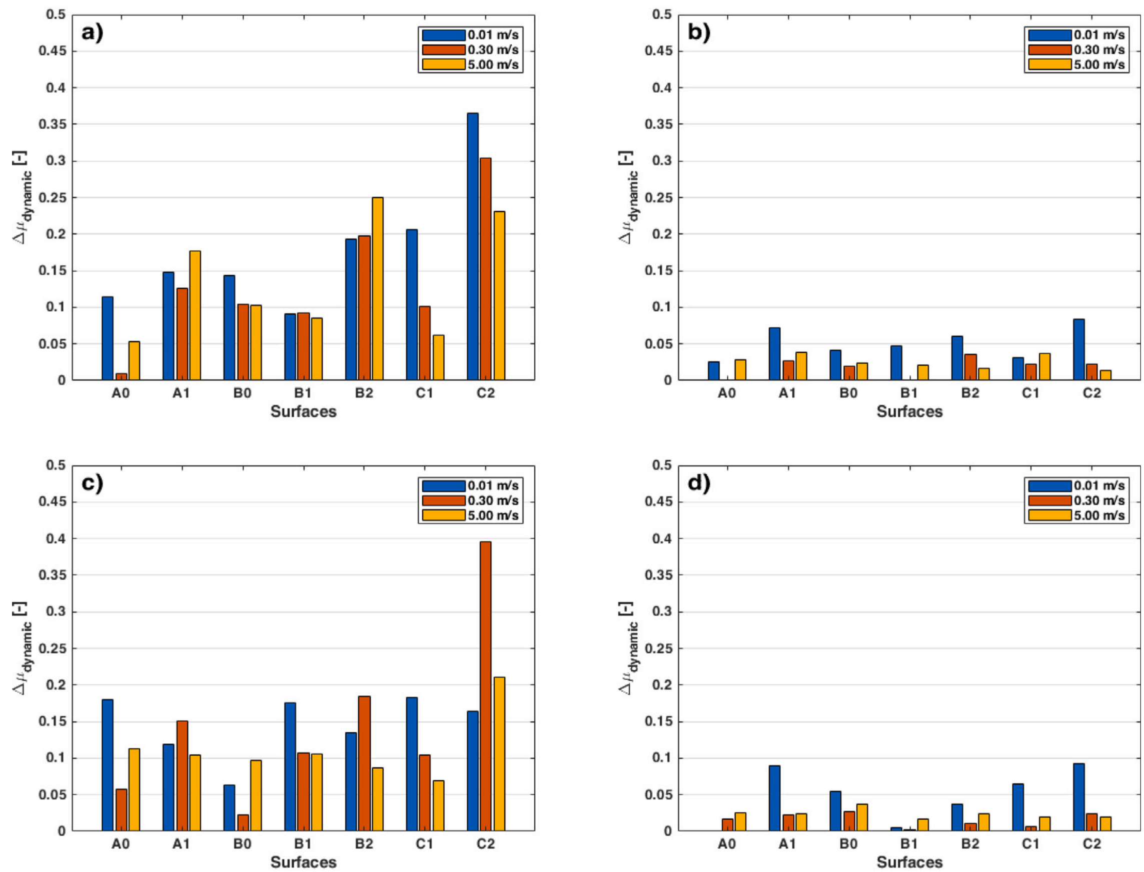

Fig. 19. Decrease of the friction coefficient with increasing nominal pressure, for dry (a & c) and lubricated (b & d) and two different compounds, A (a & b) and B (c & d), at low sliding speeds (different colours).

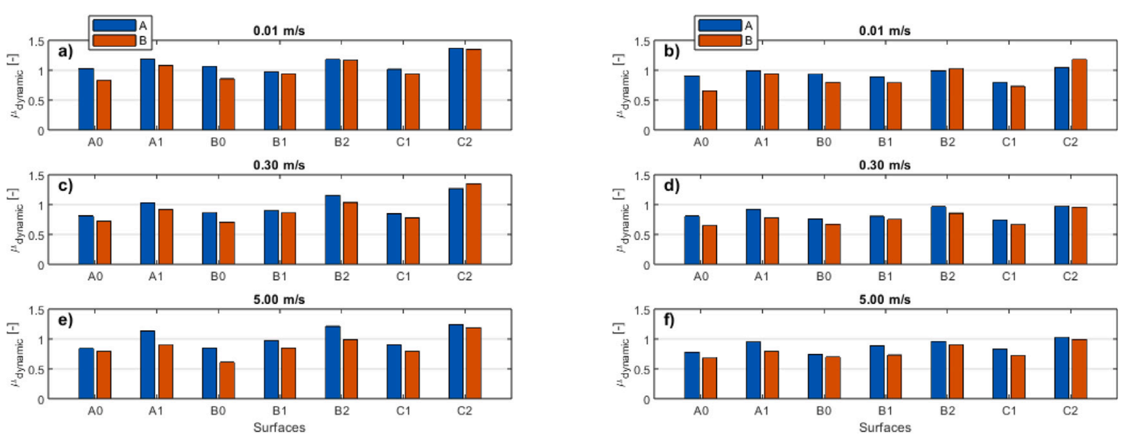

Fig. 20. Total friction coefficient comparison between two compounds A and B (different colours) for all surfaces at two nominal contact pressures: 0.15 MPa (a, c & e) and 0.30 MPa (b, d & f), at three sliding velocities, 0.01 m/s (a & b), 0.03 m/s (c & d), 0.10 m/s (e & f).

input. All other model inputs were kept unchanged. In particular, the same adhesive fitting parameters identified on the Gaussian reference surface and reported in Table 3 were retained, without any additional surface-specific calibration. Therefore, the separation among the resulting curves originates exclusively from the use of the different Top PSDs.

Fig. 25 shows that replacing the complete PSD with the Top PSD produces a pronounced separation of the predicted friction curves. This result differs substantially from the predictions obtained using the complete PSDs, for which the curves were almost indistinguishable. The Top PSD-based calculations therefore introduce a clear surface-dependent categorisation without modifying either the compound properties or the fitted adhesive parameters.

The predicted ranking is broadly consistent with the experimental observations. Surfaces C2 and B2, characterised by the lowest Top PSD levels, generally exhibit the highest predicted friction, whereas A0 and B0 remain among the surfaces with the lowest friction. The resulting order is approximately

$$C2,\ B2,\ A1,\ B1,\ C1,\ A0,\ B0,$$

which closely reflects the principal ranking observed experimentally under dry conditions.

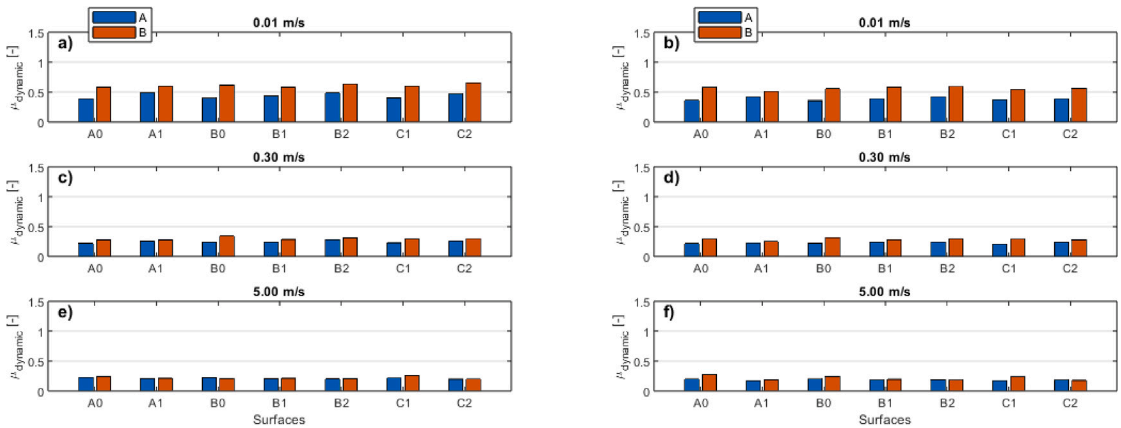

Fig. 21. Hysteretic friction coefficient comparison between two compounds A and B (different colours) for all surfaces at two nominal contact pressures: 0.15 MPa (a, c & e) and 0.30 MPa (b, d & f), at three sliding velocities, 0.01 m/s (a & b), 0.03 m/s (c & d), 0.10 m/s (e & f).

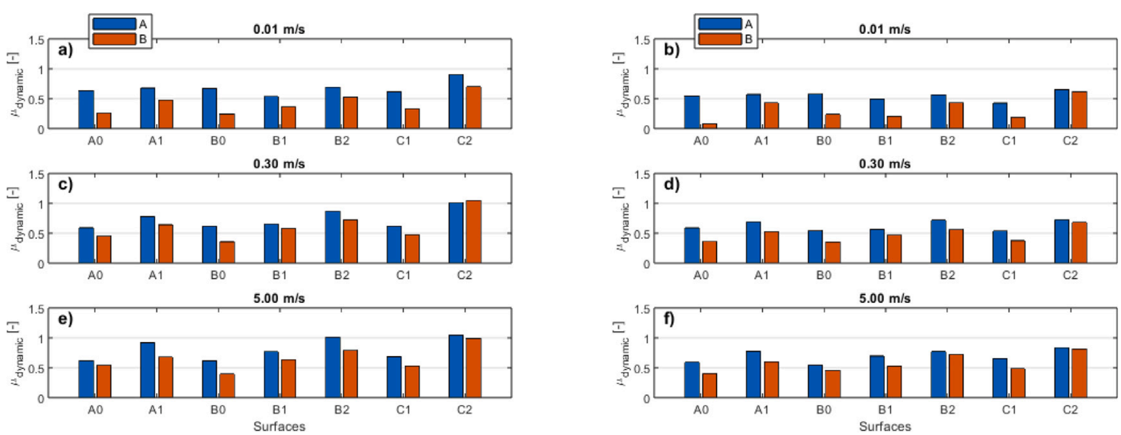

Fig. 22. Non-hysteretic friction coefficient comparison between two compounds A and B (different colours) for all surfaces at two nominal contact pressures: 0.15 MPa (a, c & e) and 0.30 MPa (b, d & f), at three sliding velocities, 0.01 m/s (a & b), 0.03 m/s (c & d), 0.10 m/s (e & f).

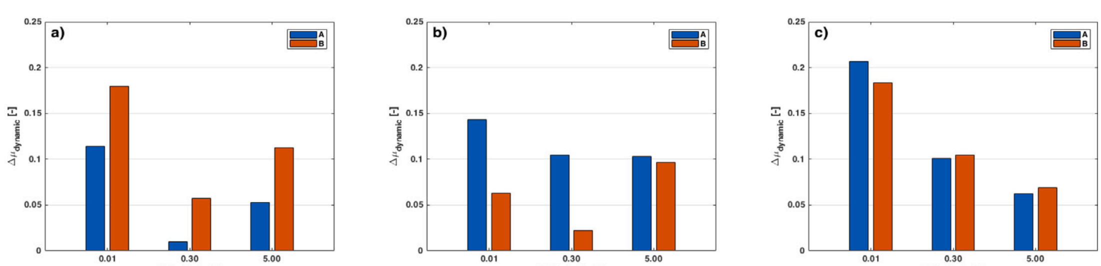

Fig. 23. Surfaces A0 (a), B0 (b), and C1 (c) with identical PSDs exhibit *different* load-induced drops in friction for compounds A and B, revealing morphology-dependent saturation.

The correspondence is particularly stable for Compound B, for which the relative order of the surfaces remains clearly distinguishable over most of the investigated velocity range at both nominal pressures. For Compound A, the same general categorisation is observed at low and intermediate sliding velocities, although small inversions and progressive convergence of some curves occur as velocity increases.

The substantial improvement obtained by introducing the Top PSD is physically significant. It suggests that the experimentally observed surface ranking is associated with the portion of the morphology effectively involved in contact, rather than with the complete spectral content considered without distinction between contacting and non-contacting regions.

7.2. Numerical and experimental investigation of real contact area

The Top PSD analysis presented in the previous subsection suggests that surfaces sharing the same full-spectrum PSD may nevertheless differ in the portion of surface effectively involved in contact. Motivated by this observation, the evolution of the real contact area was investigated through both numerical simulations and dedicated experimental measurements. A qualitative contact mechanics analysis was first performed using a Boundary Element Method (BEM) implementation available within the open-source platform *contact.engineering* [67]. The numerical predictions were then compared with experimentally measured contact areas obtained using pressure-sensitive films under

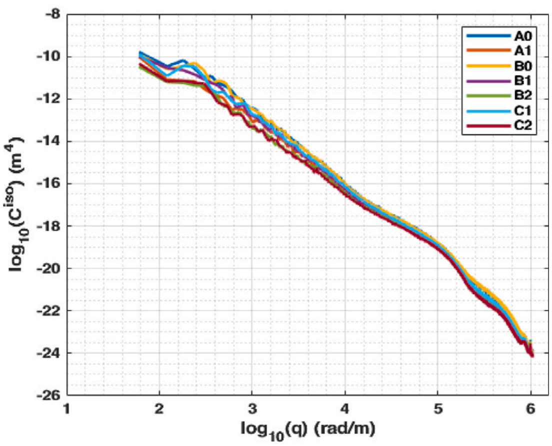

Fig. 24. Radially averaged two-dimensional Top PSDs obtained by retaining the portion of each measured surface located above its mean plane. Although the complete PSDs overlap, the Top PSDs exhibit a clear surface-dependent ranking.

the same loading conditions adopted in the friction campaign and with the friction results at the lower sliding velocity.

7.2.1. Numerical contact mechanics

The BEM platform provides FFT-accelerated elastic contact simulations for rough surfaces and implements numerical contact mechanics formulations extensively adopted in the tribology and rough-contact literature. In particular, the adopted solver computes the evolution of the contact area and pressure distribution under increasing nominal load for measured surface topographies.

The implemented approach models the contact between a rigid rough surface and an elastic half-space under frictionless normal loading conditions. The elastic problem is solved through a Fourier-based Boundary Element Method (BEM), following formulations widely adopted for rough-contact simulations [68–70]. The method assumes linear elastic behaviour and evaluates the normal displacement field induced by the surface pressure distribution.

In the present work, the simulations were not intended to quantitatively predict friction coefficients. Instead, they were employed as a qualitative tool to investigate whether surfaces characterised by identical PSDs but different height distributions (PDFs) could exhibit different evolutions of the real contact area with load.

This point is particularly relevant because classical spectrum-based approaches primarily relate contact mechanics quantities to the surface PSD, whereas the experimental results presented in this work suggest that the statistical height distribution may additionally influence contact saturation and, consequently, the load sensitivity of friction.

The simulations were performed at the same nominal pressures adopted in the experimental campaign. The normalised pressure values p/E^* were computed using the nominal contact pressures and the reduced elastic modulus of each rubber compound evaluated at the test temperature and excitation frequency adopted in the viscoelastic characterisation.

For Compound B, the investigated normalised pressures correspond to $p/E^* = 0.0235$ and 0.0470, whereas for Compound A the corresponding values are 0.0980 and 0.1960. The large difference between the normalised pressures of the two compounds originates from their different reduced elastic modulus, reflecting the distinct viscoelastic stiffness of the investigated materials.

Fig. 26 shows the evolution of the normalised BEM-calculated contact area as a function of normalised nominal pressure for the investigated surfaces. Although all surfaces share the same PSD, the numerical simulations reveal systematic differences in contact-area evolution and contact saturation behaviour.

In particular, some surfaces exhibit a faster increase of contact area at low loads and a stronger tendency towards contact saturation, whereas others maintain a more gradual contact evolution over the investigated pressure range. Importantly, these differences remain coherent and systematic across the entire loading range, suggesting that they originate from intrinsic morphological differences associated with the height distribution rather than from numerical scatter.

Although the simulations are purely elastic and do not include viscoelastic dissipation mechanisms, adhesion, sliding effects, or frictional heating (flash-temperature effects), the observed differences support the hypothesis that the statistical height distribution can influence the evolution of the contact area even when the spectral content remains unchanged. Consequently, the numerical results should be interpreted as a qualitative investigation of contact mechanics rather than as a quantitative prediction of rubber friction.

Overall, the BEM analysis provides numerical evidence supporting the hypothesis suggested by both the Top PSD analysis and the experimental friction measurements: surfaces sharing the same PSD but different PDFs may develop different real contact areas under identical loading conditions. Nevertheless, numerical predictions alone are insufficient to verify whether such differences effectively occur in real rubber–surface contact. For this reason, experimental measurements of the contact area were carried out using pressure-sensitive films under the same loading conditions adopted for the friction experiments.

7.2.2. Experimental contact area measurements

To experimentally verify whether surfaces sharing the same PSD develop different real contact areas under identical loading conditions, dedicated static contact measurements were carried out using Fuji Prescale pressure-sensitive films. The tests were performed using the GRIP test bench [71] located at the University of Naples “Federico II”, operated in a static loading configuration. The rubber specimen was conditioned before each measurement and subsequently allowed to rest for 60 s. The nominal load was then applied for 60 s while maintaining the test temperature at 30°C. The measurements were repeated for both rubber compounds, both nominal contact pressures (0.15 and 0.30 MPa), and all seven investigated surfaces.

A Fuji Prescale Ultra Super Low Pressure (LLLW) film, characterised by an operating pressure range of approximately 0.2–0.6 MPa, was positioned between the rubber specimen and the investigated surface. The film consists of two pressure-sensitive layers containing microcapsules that rupture under compression, producing a coloured imprint proportional to the local contact pressure. Fig. 27 illustrates the experimental procedure before and after the application of the nominal load.

After loading, the developed films were digitised under identical scanning conditions and processed through an automatic image-analysis procedure. The contact regions were segmented using Otsu’s thresholding algorithm, allowing the real-to-nominal contact-area ratio A_c/A_0 to be calculated from the fraction of pixels belonging to the coloured imprint. The resulting value represents the apparent contact area developed during the prescribed static loading interval.

Fig. 28 reports the experimentally measured real contact-area ratios for the two compounds and the two nominal contact pressures. Although all the investigated surfaces share the same complete PSD, systematic differences in the contact area are clearly observed under every testing condition.

For Compound A, the measured contact area varies substantially among the different surfaces, ranging from approximately 47% for surface B0 up to approximately 80% for surface C2 at the lower nominal pressure. Increasing the nominal pressure enlarges the contact area for all surfaces, although the magnitude of this increase depends on the surface morphology.

Compound B exhibits systematically smaller contact areas than Compound A, consistently with its higher stiffness. Nevertheless, the

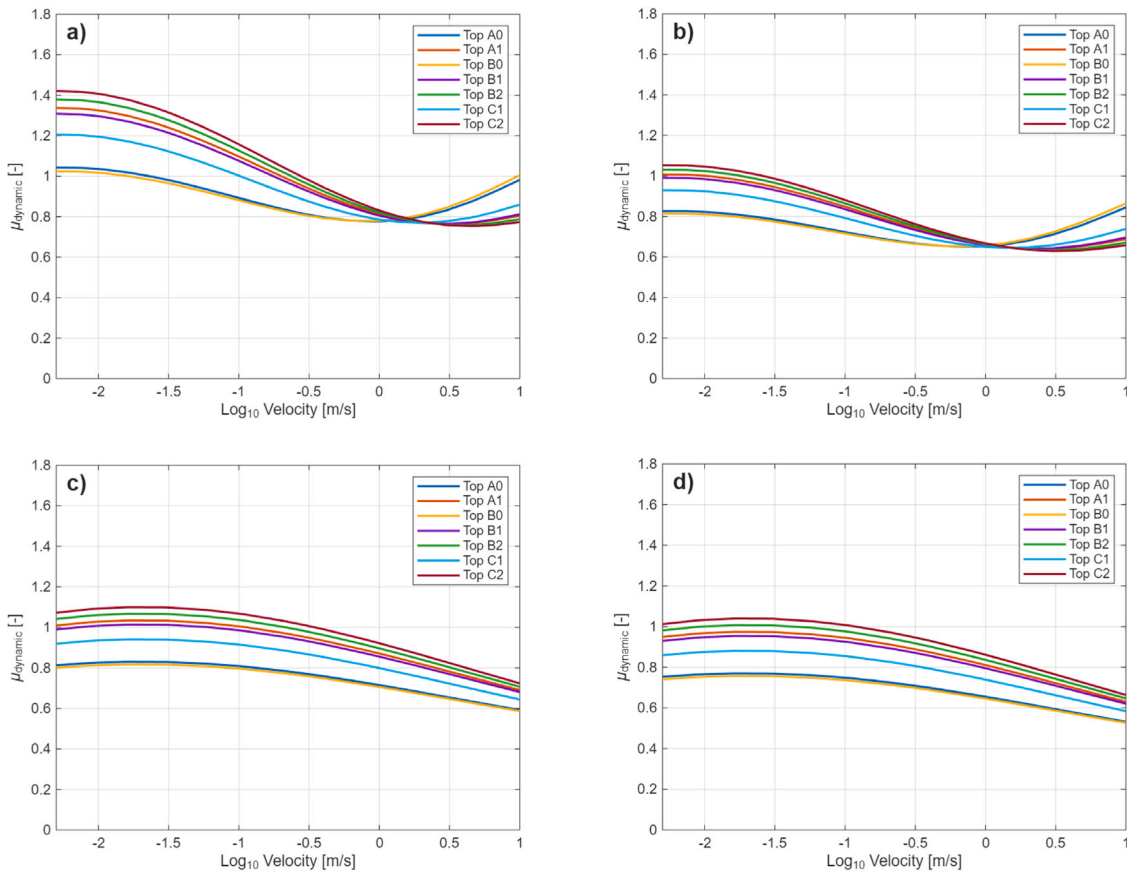

Fig. 25. Friction predictions obtained using Persson's model with the measured Top PSDs as spectral input and the same fitting parameters reported in Table 3. Results are shown for Compound A at nominal pressures of 0.15 MPa (a) and 0.30 MPa (b), and for Compound B at nominal pressures of 0.15 MPa (c) and 0.30 MPa (d).

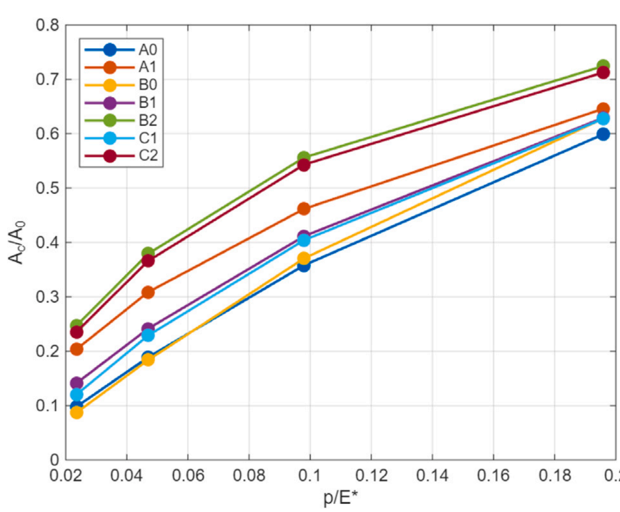

Fig. 26. Evolution of the normalised contact area A_c/A_0 as a function of normalised nominal pressure p/E^* for the investigated surfaces obtained through BEM simulations. Despite sharing the same PSD, the surfaces exhibit different contact-area evolution and different saturation tendencies with increasing load.

same morphology-dependent ranking is preserved: surfaces such as B2 and C2 develop the largest contact areas, whereas B0 and A0 consistently exhibit the smallest values.

These measurements experimentally demonstrate that surfaces sharing the same PSD do not necessarily develop the same real contact area. Instead, the statistical height distribution influences both the extent of the contact area and its evolution with increasing nominal pressure.

Overall, the experimental measurements confirm that the investigated surfaces develop different real contact configurations despite sharing the same PSD. In the following subsection, these measurements are directly compared with the BEM predictions and with the experimentally measured dry-friction response in order to assess the overall consistency among the three approaches.

7.2.3. Comparison between numerical predictions, experimental contact area and friction

The previous analyses independently showed that both the BEM simulations and the experimental measurements identify systematic differences in the contact area among surfaces sharing the same PSD. To assess whether these contact-mechanics differences are consistent with the experimentally observed friction behaviour, Fig. 29 directly compares the normalised contact area predicted by the BEM, the normalised contact area measured using Fuji Prescale films, and the normalised dry-friction coefficient obtained from the tribological tests at the lowest sliding velocity (10 mm/s). For illustrative purposes, the comparison is reported for Compound A at a nominal pressure of 0.15 MPa. However, the same considerations and qualitative trends apply to all the other investigated operating conditions. Each quantity, namely the BEM contact area, the experimentally measured contact area, and the dry-friction coefficient, was independently normalised by dividing the seven surface values by the maximum value of the corresponding dataset. Consequently, the highest value is equal to one, while the remaining values represent the relative variation among the investigated surfaces. This normalisation removes differences in absolute scale and

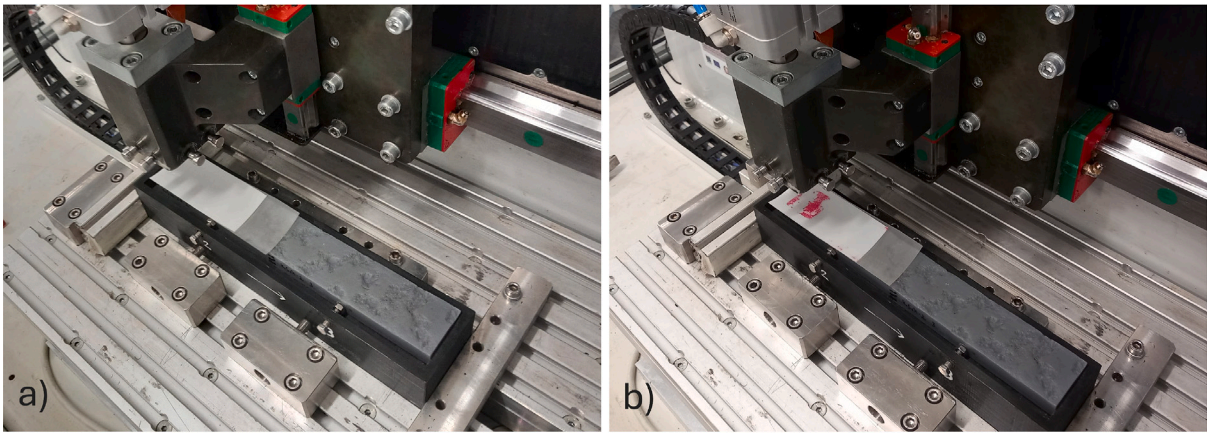

Fig. 27. Experimental procedure adopted for the static contact measurements using Fuji Prescale Ultra Super Low Pressure (LLLW) film: (a) pressure-sensitive film before loading; (b) developed film after loading, where the coloured imprint identifies the regions involved in real contact.

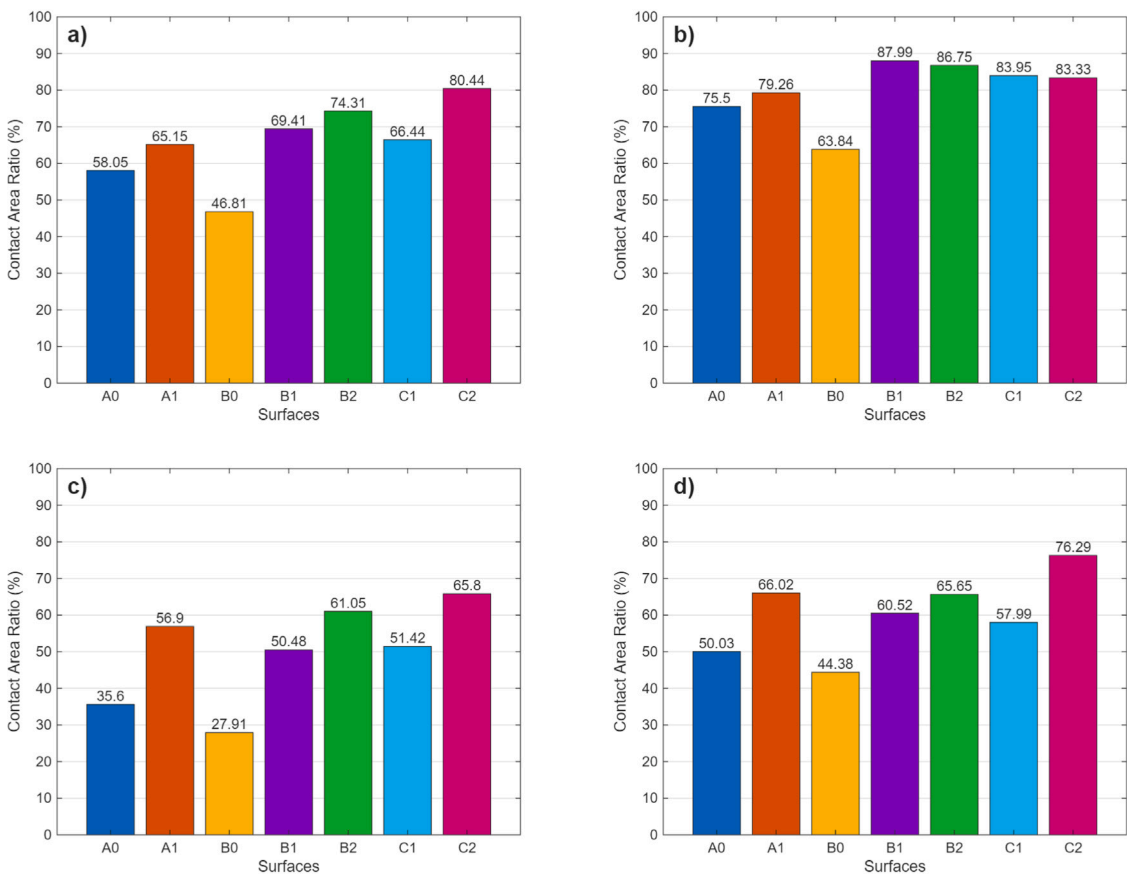

Fig. 28. Experimentally measured real contact-area ratio after a conditioning procedure followed by a resting time of 60 s. Results are shown for Compound A at nominal pressures of (a) 0.15 MPa and (b) 0.30 MPa, and for Compound B at nominal pressures of (c) 0.15 MPa and (d) 0.30 MPa.

allows the comparison to focus exclusively on the relative ranking of the surfaces.

An overall qualitative consistency clearly emerges among the three independent datasets. Surfaces predicted by the BEM model to develop larger contact areas generally also exhibit larger experimentally measured contact areas and, in turn, higher dry-friction coefficients. Likewise, surfaces characterised by smaller contact areas consistently produce lower friction levels. Although local deviations remain, the overall surface ranking is largely preserved across the numerical predictions, the experimental contact measurements, and the tribological results.

It should be emphasised that the purpose of this comparison is not to establish a direct proportionality between friction and contact area, nor to quantitatively validate the BEM model. The numerical simulations describe frictionless contact between a rigid rough surface and a linear elastic half-space, whereas the experimental measurements involve finite film thickness, viscoelastic rubber deformation, stress relaxation, pressure-sensitive film response, and static loading. Furthermore, the friction measurements additionally include adhesion, viscoelastic dissipation, sliding-induced deformation and frictional heating. Consequently, quantitative agreement among the three quantities cannot be expected.

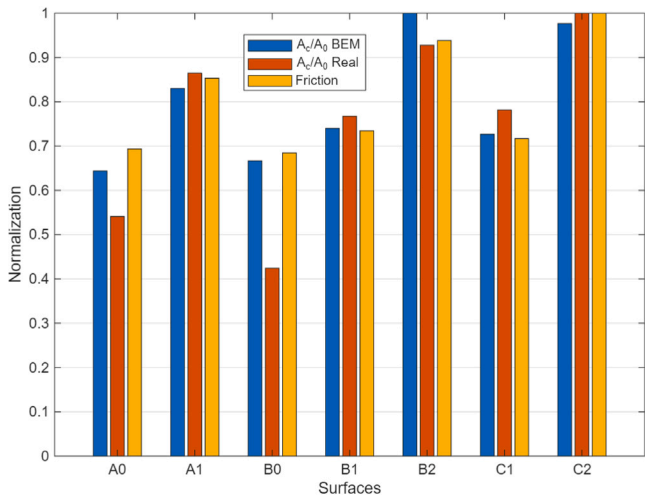

Fig. 29. Comparison between the normalised contact area predicted by the BEM simulations, the normalised contact area experimentally measured using Fuji Prescale Ultra Super Low Pressure (LLLW) films, and the normalised dry-friction coefficient for Compound A at the nominal pressure of 0.15 MPa and sliding velocity of 10 mm/s. All quantities were independently normalised with respect to the maximum value of the corresponding dataset.

Nevertheless, the fact that three completely independent approaches converge towards the same qualitative surface ranking provides strong physical support for the interpretation proposed throughout this work. The Top PSD analysis suggests that the effective roughness participating in contact differs among the investigated surfaces; the BEM simulations predict different evolutions of the contact area despite identical PSDs; the pressure-sensitive measurements experimentally confirm that these surfaces indeed develop different contact configurations; and the friction measurements consistently follow the same tendency.

8. Conclusion

In this study, we experimentally compared rubber friction on surfaces sharing the same PSD but differing in their PDF to investigate the adequacy of spectrum-based descriptions of rubber friction. Using a hybrid generation method (FFT+Johnson), we produced seven samples with overlapping PSDs (Fig. 7) but varied kurtosis and skewness (Fig. 8), thereby isolating the effect of asperity morphology independent of the spectral content.

Dry-contact tests revealed substantial variations in the total friction coefficient μ_{tot} among samples (Fig. 14), despite identical PSDs. When the data were normalised with respect to the Gaussian reference surface (A0) (Fig. 15), these differences became even more evident, demonstrating that the statistical height distribution (PDF) plays a significant role in governing the overall frictional response in addition to the spectral content captured by the PSD.

Under boundary-lubricated conditions (Fig. 16), the friction coefficients were nearly identical across all surfaces, confirming that the hysteretic contribution μ_{hyst} is predominantly governed by the spectral content (PSD). This behaviour is consistent with spectrum-based models, which predict that surfaces sharing the same PSD exhibit similar hysteretic losses. In contrast, as seen in the dry-contact results (Fig. 14), clear differences in the total friction coefficient μ_{tot} arise, indicating that the non-hysteretic (contact) component μ_{cont} is strongly affected by surface morphology and height distribution.

Taken together, the dry and lubricated experiments provide a coherent interpretation of the friction mechanisms. The hysteretic contribution is satisfactorily described through the PSD alone, whereas the remaining differences observed under dry conditions originate from the contact-related contribution, which is strongly influenced by the statistical height distribution. These deviations are systematic and surface-specific, indicating a genuine morphological effect rather than experimental scatter.

The comparison with Persson's theory further supports this interpretation. When the model is calibrated on the Gaussian reference surface (A0) and subsequently applied without further adjustment to the remaining surfaces, it correctly reproduces the overall velocity dependence and predicts nearly identical hysteretic contributions for surfaces sharing the same PSD, but it fails to reproduce the experimentally observed dry-friction ranking. The same theoretical framework was then implemented using the experimentally measured Top PSD. Although this approach introduces a surface-dependent categorisation that qualitatively follows the experimental ranking, its application requires an estimate of the portion of the surface roughness that is effectively involved in contact. This aspect is conceptually important, since the frictional response is governed not by the entire surface morphology, but by the subset of asperities that actually participate in the contact interaction. In the present analysis, this portion was approximated using the mean plane as the selection criterion. The resulting Top PSD should therefore be interpreted as a physically motivated, first-order representation of the effective contact morphology rather than as an exact reconstruction of the real contact interface.

To investigate the physical origin of these discrepancies, the theoretical analysis was complemented by numerical and experimental contact-mechanics investigations.

The qualitative Boundary Element Method (BEM) simulations further reinforced this interpretation. Although the adopted formulation neglects viscoelastic dissipation, adhesion, sliding and flash-temperature effects, it consistently predicted different evolutions of the real contact area for surfaces sharing identical PSDs but different height distributions. The simulations therefore demonstrate that the statistical distribution of surface heights alone is sufficient to generate different contact formation and saturation behaviours, even under identical loading conditions.

These numerical predictions were subsequently compared with direct measurements of the contact area obtained using Fuji Prescale Ultra Super Low Pressure (LLLW) films. The experimental measurements confirmed that the investigated surfaces develop systematically different contact areas depths despite sharing the same complete PSD. The experimentally observed ranking was found to be in good qualitative agreement with the BEM predictions, providing independent support for the proposed contact-mechanics interpretation.

Finally, the comparison between the experimentally measured contact areas, the numerical BEM predictions and the dry-friction measurements revealed a consistent qualitative correspondence among all three quantities. Although no direct proportionality is expected, because each approach relies on different simplifying assumptions and is subject to its own limitations of validity, they independently identify essentially the same surface-dependent trend. This convergence strongly supports the conclusion that the experimentally observed dry-friction variability originates from PDF-induced modifications of real contact formation and contact saturation, rather than from differences in spectral content alone.

Overall, the combined theoretical, numerical and experimental analyses establish a coherent physical framework linking surface morphology to friction. The complete PSD correctly describes the viscoelastic (hysteretic) contribution, the Top PSD provides a better approximation of the portion of roughness effectively involved in contact, the BEM simulations predict different contact-area evolutions arising from different height distributions, and the pressure-sensitive film measurements experimentally validate these differences. Taken together, these observations suggest that, under dry-contact conditions, the real contact area—although intrinsically difficult to determine rigorously—appears to be the primary parameter governing the experimentally observed friction ranking.

CRediT authorship contribution statement

Stefano Avolio: Writing – original draft, Visualization, Validation, Software, Methodology, Investigation, Data curation. **Matthias Wangenheim:** Writing – review & editing, Supervision, Resources, Methodology, Conceptualization. **Andrea Ronchi:** Writing – review & editing, Supervision, Formal analysis, Data curation. **Antonio Serra:** Validation, Software, Resources, Methodology, Investigation, Data curation. **Francesco Timpone:** Writing – review & editing, Visualization, Validation, Formal analysis. **Andrea Genovese:** Writing – original draft, Supervision, Project administration, Methodology, Formal analysis, Conceptualization.

Declaration of competing interest

The authors declare that they have no known competing financial interests or personal relationships that could have appeared to influence the work reported in this paper.

Data availability

Data will be made available on request.

References

[1] Leach R. Introduction to surface topography. In: Characterisation of areal surface texture. Berlin, Heidelberg: Springer Berlin Heidelberg; 2013, p. 1–13. http://dx.doi.org/10.1007/978-3-642-36458-7_1.
[2] Barquins M. Adherence, friction and wear of rubber-like materials. Wear 1992;158(1–2):87–117.
[3] Kluppel M, Heinrich G. Rubber friction on self-affine road tracks. Rubber Chem Technol 2000;73(4):578–606.
[4] Persson BN, Albohr O, Tartaglino U, Volokitin AI, Tosatti E. On the nature of surface roughness with application to contact mechanics, sealing, rubberfriction and adhesion. J Phys: Condens Matter 2004;17(1):R1.
[5] Carbone G, Lorenz B, Persson BN, Wohlers A. Contact mechanics and rubber friction for randomly rough surfaces with anisotropic statistical properties. Eur Phys J E 2009;29:275–84.
[6] Aghababaei R, Warner DH, Molinari J-F. Critical length scale controls adhesive wear mechanisms. Nat Commun 2016;7(1):11816.
[7] Frérot L, Aghababaei R, Molinari J-F. A mechanistic understanding of the wear coefficient: From single to multiple asperities contact. J Mech Phys Solids 2018;114:172–84.
[8] Persson B, Xu R, Miyashita N. Rubber wear: experiment and theory. J Chem Phys 2025;162(7).
[9] Barquins M, Roberts A. Rubber friction variation with rate and temperature: some new observations. J Phys D: Appl Phys 1986;19(4):547.
[10] Persson BN. Rubber friction: role of the flash temperature. J Phys: Condens Matter 2006;18(32):7789.
[11] Lang A, Klüppel M. Influences of temperature and load on the dry friction behaviour of tire tread compounds in contact with rough granite. Wear 2017;380:15–25.
[12] Do M-T, Cerezo V. Road surface texture and skid resistance. Surf Topogr: Metrol Prop 2015;3(4):043001.
[13] Chen S, Liu X, Luo H, Yu J, Chen F, Zhang Y, Ma T, Huang X. A state-of-the-art review of asphalt pavement surface texture and its measurement techniques. J Road Eng 2022;2(2):156–80.
[14] Farroni F, Russo R, Timpone F. Experimental investigations on rubber friction coefficient dependence on visco-elastic characteristics, track roughness, contact force, and slide velocity. Tire Sci Technol 2017;45(1):3–24.
[15] Arricale VM, Sammartino A, Napolitano Dell'Annunziata G, Timpone F. RIDElab: Advanced calibration tool for a real-time MF-based multiphysical tire model. AIP Publ 2023;2872(1).
[16] Arricale VM, Genovese A, Farroni F, Maiorano A, Mosconi L, Sakhnevych A, Timpone F. Experimental friction analysis through innovative compound-substrate contact modeling for automotive applications. AIP Publ 2023;2872(1).
[17] Zhang M, Yin H, Tan J, Wang X, Yang Z, Hao L, Du T, Niu Z, Ge Y. A comprehensive review of tyre wear particles: Formation, measurements, properties, and influencing factors. Atmos Environ 2023;297:119597.
[18] De Oliveira T, Muresan B, Ricordel S, Lumière L, Truong X-T, Poirier L, Gasperi J. Realistic assessment of tire and road wear particle emissions and their influencing factors on different types of roads. J Hazard Mater 2024;465:133301.
[19] Muresan B, Cesbron J, Lumière L, Gary V, Truong X-T, Kane M. A study of the relationship between rear-of-wheel particle emissions and close-proximity tire/road noise of a passenger car. Sci Total Environ 2024;918:170578.
[20] Persson BN. Theory of rubber friction and contact mechanics. J Chem Phys 2001;115:3840–61. http://dx.doi.org/10.1063/1.1388626.
[21] Chaudhury MK, Owen MJ. Adhesion hysteresis and friction. Langmuir 1993;9(1):29–31.
[22] Wang A, Zhou Y, Müser MH. Modeling adhesive hysteresis. Lubricants 2021;9:1–30. http://dx.doi.org/10.3390/lubricants9020017.
[23] Carbone G, Mandriota C, Menga N. Theory of viscoelastic adhesion and friction. Extrem Mech Lett 2022;56. http://dx.doi.org/10.1016/j.eml.2022.101877.
[24] Persson BN, Volokitin AI. Rubber friction on smooth surfaces. Eur Phys J E 2006;21:69–80. http://dx.doi.org/10.1140/epje/i2006-10045-9.
[25] Popov VL. Rubber friction and contact mechanics of rubber. In: Contact mechanics and friction. Springer Berlin Heidelberg; 2010, p. 255–70. http://dx.doi.org/10.1007/978-3-642-10803-7_16.
[26] Gal AL, Klüppel M. Investigation and modelling of rubber stationary friction on rough surfaces. J Phys Condens Matter 2008;20. http://dx.doi.org/10.1088/0953-8984/20/01/015007.
[27] Carbone G, Putignano C. A novel methodology to predict sliding and rolling friction of viscoelastic materials: Theory and experiments. J Mech Phys Solids 2013;61:1822–34. http://dx.doi.org/10.1016/j.jmps.2013.03.005.
[28] Fortunato G, Ciaravola V, Furno A, Scaraggi M, Lorenz B, Persson BN. Dependency of rubber friction on normal force or load: theory and experiment. Tire Sci Technol 2017;45(1):25–54.
[29] Pawlus P, Reizer R, Wieczorowski M. A review of methods of random surface topography modeling. 2020, http://dx.doi.org/10.1016/j.triboint.2020.106530.
[30] Hu YZ, Tonder K. Simulation of 3-D random rough surface by 2-D digital filter and Fourier analysis. Int J Mach Tools Manulact 1992;32:83–90. http://dx.doi.org/10.1016/0890-6955(92)90064-N.
[31] Wu J-J. Simulation of rough surfaces with FFT. Tribol Int 2000;33:47–58. http://dx.doi.org/10.1016/S0301-679X(00)00016-5, URL www.elsevier.com/locate/triboint.
[32] Pérez-Ràfols F, Almqvist A. Generating randomly rough surfaces with given height probability distribution and power spectrum. Tribol Int 2019;131:591–604. http://dx.doi.org/10.1016/j.triboint.2018.11.020.
[33] Nayak PR. Random process model of rough surfaces. J Lubr Technol 1971;93(3):398–407. http://dx.doi.org/10.1115/1.3451608, arXiv:https://asmedigitalcollection.asme.org/tribology/article-pdf/93/3/398/5513190/398_1.pdf.
[34] Davis BR, Thompson A. Power spectral density of road profiles. Veh Syst Dyn 2001;35(6):409–15.
[35] Jacobs TD, Junge T, Pastewka L. Quantitative characterization of surface topography using spectral analysis. Surf Topogr: Metrol Prop 2017;5(1):013001. http://dx.doi.org/10.1088/2051-672X/aa51f8.
[36] Tolpekina TV, Persson BN. Adhesion and friction for three tire tread compounds. 2019, http://dx.doi.org/10.3390/lubricants7030020.
[37] Van Loan C. Computational Frameworks for the Fast Fourier Transform. SIAM; 1992.
[38] Heinrich G. Hysteresis friction of sliding rubbers on rough and fractal surfaces. Rubber Chem Technol 1997;70(1):1–14. http://dx.doi.org/10.5254/1.3538415.
[39] Wagner P, Wriggers P, Klapproth C, Prange C, Wies B. Multiscale FEM approach for hysteresis friction of rubber on rough surfaces. Comput Methods Appl Mech Engrg 2015;296:150–68. http://dx.doi.org/10.1016/j.cma.2015.08.003, URL https://www.sciencedirect.com/science/article/pii/S0045782515002492.
[40] Bhushan B. Surface roughness analysis and measurement techniques. In: Modern tribology handbook, two volume set. CRC Press; 2000, p. 79–150.
[41] Bhushan B. Principles and applications of tribology. John Wiley & Sons; 2013.
[42] Whitehouse DJ. Handbook of surface metrology. Routledge; 2023.
[43] Gadelmawla ES, Koura MM, Maksoud TM, Elewa IM, Soliman HH. Roughness parameters. J Mater Process Technol 2002;123:133–45. http://dx.doi.org/10.1016/S0924-0136(02)00060-2.
[44] Kanafi MM, Tuononen AJ, Dorogin L, Persson BN. Rubber friction on 3D-printed randomly rough surfaces at low and high sliding speeds. Wear 2017;376–377:1200–6. http://dx.doi.org/10.1016/j.wear.2017.01.092.
[45] Lorenz B, Persson BN, Fortunato G, Giustiniano M, Baldoni F. Rubber friction for tire tread compound on road surfaces. J Phys Condens Matter 2013;25. http://dx.doi.org/10.1088/0953-8984/25/9/095007.
[46] Lorenz B, Oh YR, Nam SK, Jeon SH, Persson BN. Rubber friction on road surfaces: Experiment and theory for low sliding speeds. J Chem Phys 2015;142. http://dx.doi.org/10.1063/1.4919221.
[47] Genovese A, Farroni F, Papangelo A, Ciavarella M. A discussion on present theories of rubber friction, with particular reference to different possible choices of arbitrary roughness cutoff parameters. Lubricants 2019;7(10):85. http://dx.doi.org/10.3390/lubricants7100085.
[48] McCool JI. Non-Gaussian effects in microcontact. Int J Mach Tools Manuf 1992;32(1–2):115–23.

[49] Yu N, Polycarpou AA. Contact of rough surfaces with asymmetric distribution of asperity heights. J Trib. 2002;124(2):367–76.
[50] Chilamakuri SK, Bhushan B. Contact analysis of non-Gaussian random surfaces. Proc Inst Mech Eng J 1998;212(1):19–32.
[51] Zhan W, Huang P. Modeling tangential contact based on non-Gaussian rough surfaces. Proc Inst Mech Eng J 2019;233(1):51–60.
[52] Sanders T, Mavros G, Knowles J. Characterisation and generation of road surface roughness for improved tyre-road interaction models. Results Eng 2025;26. http://dx.doi.org/10.1016/j.rineng.2025.105644.
[53] Slifker JF, Shapiro SS. The Johnson system: Selection and parameter estimation. Technometrics 1980;22:239–46. http://dx.doi.org/10.1080/00401706.1980.10486139.
[54] Kanafi MM, Tuononen AJ. Application of three-dimensional printing to pavement texture effects on rubber friction. Road Mater Pavement Des 2017;18:865–81. http://dx.doi.org/10.1080/14680629.2016.1194883.
[55] Rodriguez N, Gontard L, Ma C, Xu R, Persson B. On how to determine surface roughness power spectra. Tribol Lett 2025;73(1):18.
[56] Pradhan A, Müser M, Miller N, Abdelnabe J, Afferrante L, Albertini D, Aldave D, Algieri L, Ali N, Almqvist A, et al. The surface-topography challenge: A multi-laboratory benchmark study to advance the characterization of topography. Tribol Lett 2025;73(3):110.
[57] International Organization for Standardization. ISO 25178: Geometrical product specifications (GPS) - Surface texture: Areal - part 2: Terms, definitions and surface texture parameters. 2021, International Organization for Standardization.
[58] International Organization for Standardization. ISO 8608: Mechanical vibration - Road surface profiles - Reporting of measured data. 2016, International Organization for Standardization.
[59] Hutchings IM. Leonardo da Vinci's studies of friction. Wear 2016;360–361:51–66. http://dx.doi.org/10.1016/j.wear.2016.04.019.
[60] Genovese A, D'Angelo GA, Sakhnevych A, Farroni F. Review on friction and wear test rigs: An overview on the state of the art in tyre tread friction evaluation. 2020, http://dx.doi.org/10.3390/LUBRICANTS8090091.
[61] Ripka S, Gäbel G, Wangenheim M. Dynamics of a siped tire tread block-experiment and simulation 3. Tire Sci Technol TSTCA 2008;37.
[62] Grosch K. The relation between the friction and visco-elastic properties of rubber. Proc R Soc Lond Ser A 1963;274:21–39. http://dx.doi.org/10.1098/rspa.1963.0112.
[63] Lorenz B, Persson BN, Dieluweit S, Tada T. Rubber friction: Comparison of theory with experiment. Eur Phys J E 2011;34. http://dx.doi.org/10.1140/epje/i2011-11129-1.
[64] Tiwari A, Dorogin L, Tahir M, Stöckelhuber KW, Heinrich G, Espallargas N, Persson BN. Rubber contact mechanics: adhesion, friction and leakage of seals. Soft Matter 2017;13(48):9103–21. http://dx.doi.org/10.1039/c7sm02038d.
[65] Persson BN. Contact mechanics for randomly rough surfaces. 2006, p. 201–27. http://dx.doi.org/10.1016/j.surfrep.2006.04.001.
[66] Guiggiani M, et al. The science of vehicle dynamics. Pisa, Italy: Springer Neth 2014;15:32.
[67] Röttger MC, Sanner A, Thimons LA, Junge T, Gujrati A, Monti JM, Nöhring WG, Jacobs TD, Pastewka L. Contact. engineering—Create, analyze and publish digital surface twins from topography measurements across many scales. Surf Topogr: Metrol Prop 2022;10(3):035032.
[68] Stanley H, Kato T. An FFT-based method for rough surface contact. 1997.
[69] Polonsky I, Keer L. A numerical method for solving rough contact problems based on the multi-level multi-summation and conjugate gradient techniques. Wear 1999;231(2):206–19.
[70] Pastewka L, Robbins MO. Contact area of rough spheres: Large scale simulations and simple scaling laws. Appl Phys Lett 2016;108(22).
[71] Genovese A, Dell'Annunziata GN, Lenzi E, Sakhnevych A, Timpone F, Farroni F. Development of a versatile indoor framework for the measurement of tyre compound friction and wear. Internat J Engrg Sci 2026;218:104402.